Engineering Structures 292 (2023) 116475

Contents lists available at ScienceDirect

Engineering Structures

journal homepage: www.elsevier.com/locate/engstruct

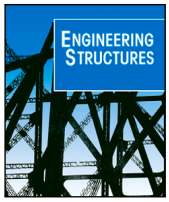

Experimental comparison of a dual-spar floating wind farm with shared mooring against a single floating wind turbine under wave conditions

Tomas Lopez-Olocco [a,b], Guodong Liang [c], Antonio Medina-Manuel [a,b], Leandro Saavedra Ynocente [d], Zhiyu Jiang [c,*], Antonio Souto-Iglesias [a,b]

[a] Universidad Politécnica de Madrid, Av. de la Memoria 4, Madrid, 28040, Spain
[b] CEHINAV, DACSON, ETSIN, Av. de la Memoria 4, Madrid, 28040, Spain
[c] Department of Engineering Sciences, University of Agder, N-4898 Grimstad, Norway
[d] Laboratorio de Dinámica del Buque, Canal de Ensayos Hidrodinámicos el Pardo (INTA-CEHIPAR), Madrid, 28040, Spain

ARTICLE INFO

Dataset link: http://canal.etsin.upm.es/papers/lopezoloccoetal_sharedmooring_2023/

Keywords:
Offshore wind farm
Spar floating wind turbine
Hydrodynamic model tests
Shared mooring
Measurement
Dynamic response

ABSTRACT

Shared mooring can potentially be a cost-reduction factor for future floating wind farms. To assess the effect of shared mooring on the response dynamics of floating wind turbines (FWTs), experiments have been conducted for two spar FWTs with a shared mooring configuration and for a single spar FWT with catenary mooring, both at a scale of 1:47. Various regular and irregular wave conditions were tested and only one wave heading was considered. From the test results, the response amplitude operators and response spectra of platform motions and statistics of mooring tensions are compared for the two configurations. In the extreme wave condition, the shared mooring configuration leads to a 40% increase in the platform surge motion compared with the single spar FWT. Still, the absolute offset is within allowable limits prescribed by power cables. The fairlead tensions of the anchor lines are not significantly increased in the shared mooring configurations, but the shared line shows extreme tension peak events that are seldom present in the anchor lines. This study demonstrates the technological promises and challenges of a shared mooring system from an experimental perspective. Results and videos are made available and can be used to validate numerical models.

1. Introduction

With an installed capacity of 12 gigawatt (GW) in 2020 and a target of 60 GW of installed capacity by 2030, the European Union aims to position herself as a leader in clean technologies [1]. To reach this objective in the next years, using conventional bottom-fixed substructures in depths below 50 m may not be sufficient. For offshore sites with deep water and convenient wind conditions, bottom-fixed platforms are unfeasible from an economic point of view. Therefore, floating offshore wind installations have the potential to expand in the near future, making them a pillar of Europe's research and development agenda [2].

Among different floating wind turbine (FWT) concepts [3], the spar FWT is one of the most technically mature and widely studied, as shown by the Hywind Demo project [4]. A spar buoy usually has a deep draft and is ballast-stabilized. To understand physical behavior and to demonstrate technical feasibility, important experimental works of spar FWTs have been carried out in the past [5–7]. The performance of spar FWT has been compared against that of other floating concepts, e.g., semi-submersible and the tension leg platform FWTs [8–10]. Generally, in wave-only conditions, the spar FWT showed smaller surge response and larger pitch responses compared to other FWT concepts. The past experimental research on spar FWTs is interesting, but limited to a single spar FWT with catenary mooring at a certain water depth, to the authors' knowledge. There is lack of experimental work considering deepwater sites and alternative mooring configurations, especially on a farm scale.

The demand of the evolution of floating offshore wind technology implies the development of innovative floating platform substructures with reliable and cost-efficient mooring solutions. The total cost for the substructure and foundation (including moorings), assembly and installation of a floating offshore wind project was estimated to be approximately 35% [11]. As the offshore wind industry has shown growing interest in locations like the Mediterranean sea [12] where deep-water floating solutions are preferable, efforts to reduce these costs are needed in current and future offshore projects. For the mooring and anchoring system of a floating wind farm (FWF), novel solutions like shared anchor or shared mooring configurations can be considered to achieve cost reductions in material consumption and installation. Shared anchors can reduce the mooring costs for floating

* Corresponding author.
E-mail address: zhiyu.jiang@uia.no (Z. Jiang).

https://doi.org/10.1016/j.engstruct.2023.116475

Available online 10 July 2023

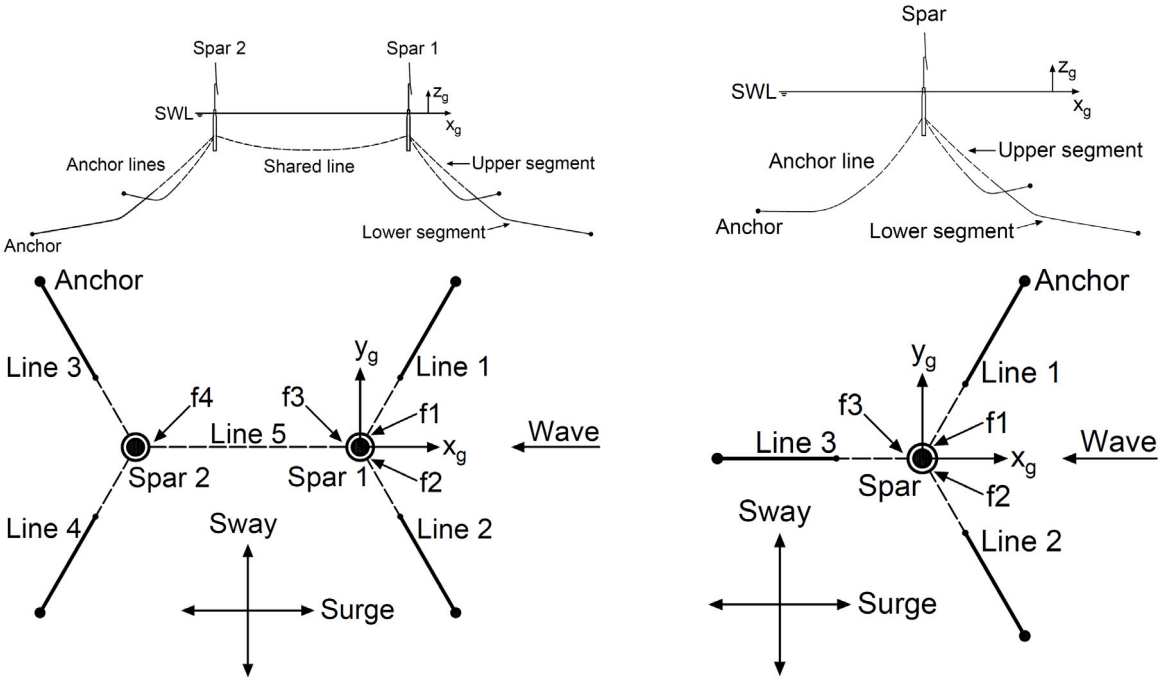

(a) Dual-spar FWF (b) Single spar FWT

Fig. 1. Top and side view of the two configurations with different mooring systems (dashed line: wire; solid line: chain). The symbols $f1$, $f2$, $f3$, $f4$ denote the fairlead connections.

wind farms by reducing the number of anchors and hence the installation costs; see [13–15]. This solution has been adopted by the Hywind Tampen FWF [16]. Shared mooring decreases the capital expenditure by reducing the total length of the mooring lines and the number of anchors [17,18], but the principles of shared mooring are yet to be further understood prior to any practical implementations.

Shared mooring systems for spar platforms have been studied in recent years in several numerical works. The elastic catenary theory for hanging cables was used to model the shared line of a dual-spar FWF [19]. In a subsequent study, Liang et al. [20] investigated the natural periods of a dual-spar FWF with a shared mooring system. The anchor lines were designed based on analysis of a single FWT. Different mooring properties were studied and a sensitivity study was performed to evaluate their contributions. The shared line showed a primary influence on the surge and sway natural periods. Liang et al. [21] further investigated the extreme response of the dual-spar FWF with a shared line through a comparison to a single spar FWT and sensitivity studies on loading directions and mooring properties of the shared line. The FWF showed larger horizontal motions and higher mooring tension in anchor lines than the single FWT. Snap events were observed in the shared line. Also, based on the mooring design of a single FWT, Wang et al. [22] proposed an array of 9 wind turbines on spars buoys in a 3-by-3 square with only eight anchors and twelve shared lines. The numerical study was intended to provide a rough estimation of cost saving in terms of number of anchors and length of mooring lines. The investigation showed larger tensions in the shared FWF than in the single FWTs for all the load cases. Wilson et al. [23] studied the optimization of shared mooring systems using a linearized model for the force–displacement relationship of floating platforms. The study showed that the more complicated the shared layout is, the greater the restoring demand for the shared lines. Similar works on FWFs can be found for floating platform concepts other than spars. For example, semi-submersibles FWF with shared mooring have been studied by Goldschmidt and Muskulus [24], Hall and Connolly [25], Connolly and Hall [26] and Lozon and Hall [27]. Overall, FWFs with shared mooring can achieve great cost reduction potentials compared with FWFs that consist of single, but larger platform motions and mooring tensions can be the trade-off.

Considering the above literature review, we observe a lack of experimental literature on the hydrodynamics of FWFs with shared mooring systems, a key aspect in validation and calibration of numerical models. To partially fill in this research gap, an experimental investigation on a dual-spar FWF with a shared mooring system is presented herein. For comparison purposes, model tests have been also conducted for a single spar FWT with a catenary mooring system. Since the focus is set on the wave-induced hydrodynamics, wind loads have not been considered.

The findings of this experimental work aim to investigate and understand the complex multibody dynamics involved in shared mooring FWFs and, hopefully, foster the development of shared-mooring concepts, with the subsequent impact on cost reduction of FWFs. To make the effort more useful to the research community, the data discussed in the paper and videos of the experiments are made available in the Data Availability section.

This paper is organized as follows. In Section 2, the case studies, the mooring system design, and the environmental conditions are presented. In Section 3, the experimental setup is described and the test matrix proposed. In Section 4, the wave calibration method and post-processing techniques that are conducted during the analysis are explained. In Section 5, the experimental results are presented and discussed. Finally, conclusions and future lines of work are enumerated.

2. Case studies

2.1. Description of the FWT and the FWF

The 5-megawatt spar FWT, OC3-Hywind [28,29], is selected in the present experimental campaign. Two different mooring configurations have been tested. As illustrated in Fig. 1, a shared mooring system is applied to the dual-spar FWF and a conventional catenary mooring system is applied to the single spar FWT. For the dual-spar FWF, two FWTs are placed along the defined surge direction. The initial turbine spacing is 750 m, which is approximately six times the rotor diameter. The static drafts of all FWTs are 120 m and all the fairleads are 70 m

Fig. 2. Top view of the model with the aluminum structure, including the instrumentation cables.

Table 1
Environmental parameters for mooring system design.

Environmental variable	Operational	Extreme
U_w (hub-height) [m/s]	11.40	42.71
H_s [m]	2.57	15.50
T_p [s]	11.12	14.45

below the still water level, the same as specified in [28]. Each FWT is moored to the seabed by two single lines through anchors (anchor lines). One shared line connects the two FWTs. The single spar FWT is connected to the seabed by three anchor lines. For both configurations, the projected angle between any neighboring mooring lines is 120 deg.

The studied water depth (235 m) of this FWT was selected considering the typical range of 200–300 m among commercial projects, e.g., Hywind Tampen [16]. Because this depth is different from the one specified in [28], a more realistic mooring design is desired. A proper redesign has been carried out with details presented in Section 2.3.

2.2. Environmental conditions

Metocean conditions of the "Norway 5" offshore site [30] are considered for the mooring design and for defining the test matrix of the experimental campaign. The joint probability distribution of the mean wind speed (U_w), the significant wave height (H_s) and the spectral peak period (T_p) is used to calculate the conditional distributions from which the mean values of H_s and T_p are taken for the operational condition. For the extreme condition, the 50-year environmental contour surface is generated based on the joint distribution. The sea state with the highest H_s on the contour surface is selected. The environmental conditions are summarized in Table 1. The wind speed is included for the sake of completeness, but wind loads were not considered in the tests.

2.3. Mooring system design

The anchor lines of the spar FWT are redesigned for the selected water depth. We follow a design process similar to the one presented in Liang et al. [20]. A two-segment mooring design is considered for the anchor lines in which the upper segment is made of sheathed steel wire rope, and the lower segment is made of a R3 studless mooring chain. The delta connection [4] is not considered for simplicity. Four design parameters are considered, including the total mooring line length, the length of the wire segment and the diameters of the wire segment and the chain segment. The design space of variables is presented in Table 2, and the orthogonal sampling method is applied. The design objective is to minimize the material costs in production and manufacturing of mooring lines. First, static analyses are performed in Mimosa [31], a program for moored vessel analysis. Then, dynamic analyses are performed in SIMA [32,33], a numerical simulation tool for marine operations and floating systems. Details of the objective function, design constraints, analysis procedures and design check can be found in Liang et al. [20]. The sample from the design space which fulfills the design constraints with the lowest mooring cost is selected as the final design for the anchor lines of the spar FWT.

Table 2
Design variables and design space of the anchor lines.

Design variable	Sampling range	Sampling interval
Total mooring line length L_{line} [m]	[660, 680]	5
Wire segment length L_{wire} [m]	[250, 350]	10
Wire segment diameter D_{wire} [mm]	[90, 130]	5
Chain segment length D_{chain} [mm]	[110, 150]	5

As shown in Fig. 1, the selected mooring properties are applied to the three mooring lines of the single spar FWT and to the four anchor lines of the dual-spar FWF. For the shared line of the dual spar FWF, steel wire rope is chosen as the material because it is lighter than chain. There is no design recommendation for the shared line design [34,35], so the same wire properties of the anchor lines are used for the shared line. Also, the length of the shared line was determined such that the distance between the platforms is equal to the target turbine spacing of approximately six times the rotor diameter in the static condition. When the floating system reaches the static equilibrium, the two FWTs are driven towards each other for a short distance due to the self weight of the shared line, leading to differences in the static pretensions between the single-spar and dual-spar configurations. The material properties of the mooring lines are summarized in Table 3.

3. Experimental setup

The experimental campaign was conducted in the ocean basin at the *Canal de Ensayos Hidrodiná- micos de el Pardo* (INTA-CEHIPAR). The dimensions of the tank are 150 m in length, 30 m in width and 5 m in depth. The tank is equipped with a towing carriage, in which the data acquisition systems reside.

As described in Section 2, the water depth of the site is 235 m. Therefore, considering the water depth of the tank, a scale ratio λ of 47 is selected.

3.1. Single FWT

When testing floating platforms in waves, gravity and inertia forces are predominant [36]. Therefore, the Froude scaling similarity laws were applied in these tests. The target model scale properties are listed in Table 4. The model was constructed with PVC plastic, and solid lead was used for the ballast. To avoid water leakage during the experiments, several seals were applied and checked before placing the model into the testing position. In addition, during the entire experimental campaign, the models were constantly inspected for water intake to avoid changes in displacement and trim angle. A detailed description of the model design is included in Appendix A.

The construction of the model resulted in errors below 5%. A comparison with the target values can be found in Table 4. The model mass was set to obtain the exact scaled draft. Errors in lengths are normalized with respect to $\nabla^{1/3}$, with ∇ being the target displacement volume.

Because the mooring lines were too lightweight, the submersible load cells could affect the mooring angle due to their elevated weight.

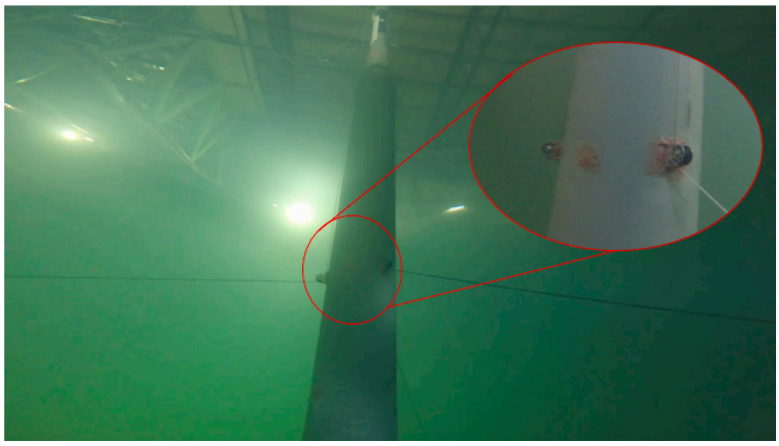

(a) Fairlead connection.

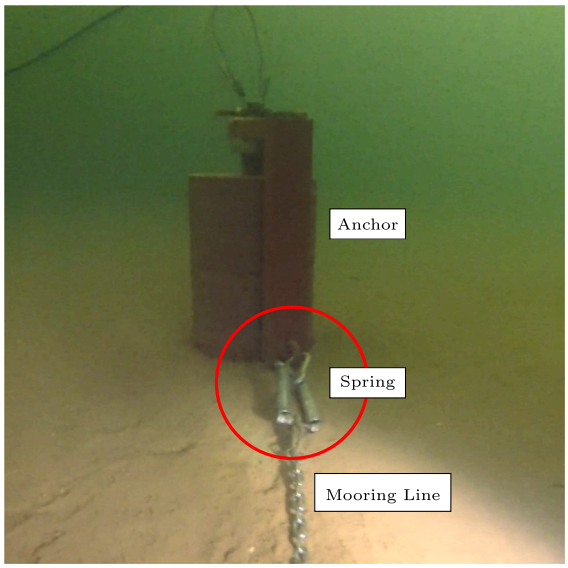

(b) Connection between the mooring line and the anchor.

Fig. 3. Mooring line connections.

Table 3
Properties of the mooring lines.

Mooring property	Anchor line		Shared line
	Lower segment	Upper segment	
Material	R3 studless chain	Sheathed steel wire rope	Sheathed steel wire rope
Length [m]	415	250	739.6
Diameter [mm]	140	95	95
Sheath thickness [mm]	–	10	10
Mass density [kg/m]	392.00	47.39	47.39
Submerged weight [N/m]	3535.94	360.42	360.42
Extensional stiffness [N]	1.53E+09	8.47E+08	8.47E+08
Minimum breaking strength [N]	1.43E+07	9.34E+06	9.34E+06

Table 4
Target and measured mass properties at model scale.

Mass property	Target value	Measured value	Units	Error
Mass	77.403	77.721	kg	0.41%
Height of COG above keel	0.894	0.891	m	0.67%
Radius of inertia about x-axis[a]	1.03	1.04	m	2.94%
Radius of inertia about y-axis[a]	1.03	1.04	m	2.95%
Radius of inertia about z-axis[a]	0.10	0.94	m	2.02%

[a]Measured with reference to center of gravity (*COG*).

Therefore, the lines are sent to the aluminum structure showed in Fig. 2 the water surface, where they were connected to the measurement devices. Pulleys were installed at the fairlead positions for that purpose. A submerged view of the fairlead connection and the pulleys used is found in Fig. 3(a). This modification forces us to consider the full pretensions instead of just the vertical component in the design process to adjust the mass properties of the model.

Special care was taken to reproduce the properties when scaling the mooring lines. The exact length was ensured and the weight per unit length of the available mooring material was chosen to be close to the ones at full scale (see Table 3). The connection parts were selected

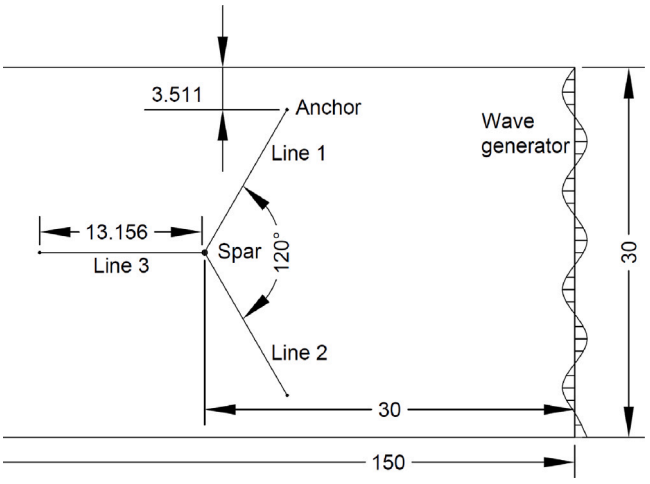

Fig. 4. Experimental layout of the single spar FWT. Dimensions at model scale [m].

Table 5
Physical properties of the mooring lines.

	Component	L [m]	w [kg/m]	K [N/m]
Anchor line	Chain	8.83	0.160	800
	Steel wire	5.32	0.020	
Shared line	Steel wire	15.736	0.020	520

Table 6
Target and measured pretensions for both configurations.

	Pretension	T_{f1}	T_{f2}	T_{f3}	T_{f4}	Units
Single spar FWT	Target	6.91	6.91	6.91	(–)	N
	Measured	6.24	6.39	5.99	(–)	N
Dual-spar FWF	Target	7.62	7.62	6.34	6.34	N
	Measured	7.97	8.04	6.78	6.67	N

to take this into account and increase the equivalent weight per unit length when needed. The resulting model scale line properties are listed in Table 5.

The number of snap events may be overpredicted if the mooring stiffness is not adequately scaled [37]. In order to have line tensions which approximately scale as the other forces involved in the system, a set of springs was placed at the anchor aiming at properly modeling the line stiffness. This connection is encircled in red in Fig. 3(b).

To select the spring, an equivalent linear stiffness of the full-scale mooring line is computed. Since the stiffness of the line should scale with λ^3 when the Froude scaling laws are applied, the linear spring stiffness, K, was selected according to Eq. (1)

$$K = \frac{EA}{L}, \tag{1}$$

where EA is the axial stiffness of the line and L is the unstretched length of the line at model scale. Results are shown in Table 5.

For the single spar FWT with catenary mooring, the model is placed 30 m away from the wave generator; see Fig. 4. In this test setup, the anchors were placed at the exact scaled positions. Also, a diver ensured the correct laying of the line at the bottom preventing the chain from crooking due to the manipulation of the chain during the installation, and conducted minor adjustments to set the pretensions prior to the tests. Table 6 shows a comparison between the measured and the target pretensions at the fairlead. Due to lack of available time in the tank, additional static tests to estimate the stiffness in the various degrees of freedom were not carried out. They are left for future work.

Table 7
Summary of test cases with irregular and regular waves.

(a) Irregular wave		
	H_s [m]	T_p [s]
Operational (IRR01)	2.57	11.12
Extreme (IRR02)	12.70	15.45
White noise (WN)	2.00	5–20
(b) Regular		
	H [m]	T [s]
REG01	2.5	5.48
REG02	2.5	9.60
REG03	2.5	10.97
REG04	5.0	8.0
REG05	10.0	16.0

3.2. Dual-spar FWF

In the dual-spar FWF, two FWTs with the same physical properties described in Section 3.1 are used. To scale down the mooring lines and their properties for this configuration, the same procedure described in Section 3.1 is followed. The layout of the mooring system of this configuration is detailed in Fig. 5.

The downscaled mooring properties and a comparison between the target and measured pretensions are listed in Tables 5 and 6. To check the installation accuracy, the distance between models was measured several times at the position of static equilibrium with a mean value of 16.054 m.

3.3. Test matrix

In total, 28 tests were carried out in this study, consisting of six decay tests, two irregular wave cases, one white noise case, and five regular wave cases for each configuration. For the wave cases, the amplitudes and periods described in Section 2.2 were scaled down according to the Froude scaling laws.

Due to the mechanical limitations of the wave generator with the selected scale ratio, the environmental conditions for irregular wave cases described in Section 2.2 were modified and listed in Table 7a, where the white noise case is also listed. The set of regular wave cases, listed in Table 7b covers both operational and extreme conditions.

3.4. Instrumentation

All measuring instruments were calibrated prior to testing to ensure quality and reliability of the data acquisition system. Measurements

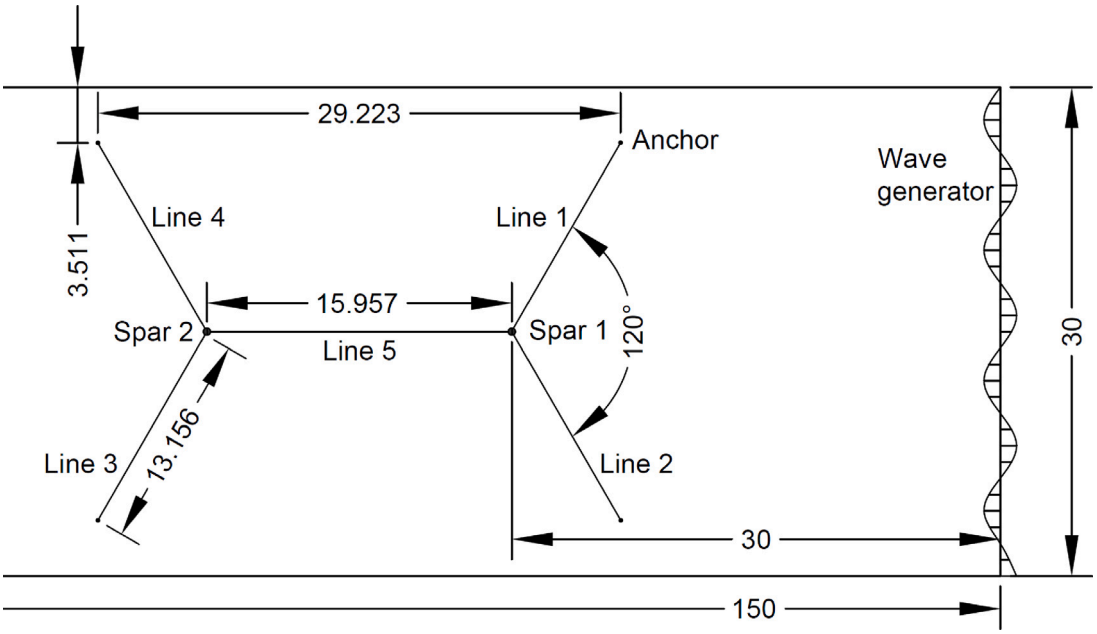

Fig. 5. Experimental layout of the dual-spar FWF. Dimensions at model scale [m].

(a) Spar 1 with all the instrumentation. (b) Spar 2 with all the instrumentation.

Fig. 6. The two spar models in testing position with the instrumentation circled in red.

were recorded with a sampling rate of 100 Hz, which was sufficient considering typical frequencies of the phenomena involved (maximum 1.2 Hz). Fig. 6 shows the sensor positions during the experiments of the dual-spar FWF. The instrumentation setup for the single FWT is identical to Spar 1 of the FWF.

In this work, the 6 degrees of freedom (DOF) rigid body motions of the model placed 30 m from the wave generator were measured using an optical tracking system, KRYPTON. The system is a camera-based dynamic position measurement of the location of one or more infrared LEDs. The frame equipped with the LEDs was attached to the model on top of the aluminum structure. In Figs. 7(a)–7(b), the lead frame and the cameras that point to Spar 1 are encircled in red. The measured motions must be further post-processed to obtain the motions of the model's COG.

For the dual-spar configuration, the fairlead tensions of the two anchor lines of Spar 1 and the tensions of the shared line at both ends are measured with four load cells. For the single spar configuration, all three mooring tensions are measured. Four one-component load cells HBM with a SGfull bridge were used. The measured range of the load cell is 0 to 200 N and the precision is ± 0.081 N based on the residual values of its calibration. The load cell was covered with an insulating material to prevent drift caused by the environment

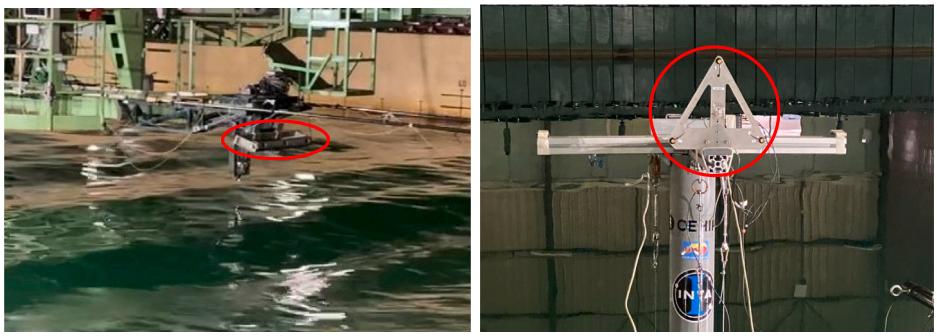

(a) Optical tracking camera. (b) Lead frame.

Fig. 7. Detailed view of the instruments used for motion measurement during the tests.

(a) Detailed view of one of the load cells with the turnbuckle. (b) Detailed view of the line arrangement.

Fig. 8. Detailed view of the load used during the tests and the line arrangement.

(a) Capacitance wave probe. (b) Ultrasonic wave probe.

Fig. 9. Detailed view of the instruments for measurements of water surface elevation.

during the experiments. A detailed view of the sensor can be seen in Fig. 8(a). A load cell, a turnbuckle for fine adjustment of the target pretension, and a steel wire connected to the catenary line are used. The arrangement can be seen in Fig. 8(b).

The incoming waves were measured by means of an ultrasonic wave sensor located in the carriage. In addition, a capacitance wave probe is used to measure the wave elevation next to Spar 2. The precision of the measuring devices is ± 2.027 mm on average. These sensors are shown in Figs. 9(a) and 9(b).

4. Methodology

4.1. Decay tests

To determine the natural periods of the platform with the mooring system designed, decay tests were performed in 6 DOFs of a single spar. The model was manually displaced from equilibrium and then released. The initial and last transient cycles are discarded for each test. Then, the remaining half cycles are analyzed. In the following, the subscript i refers to the ith-half cycle, starting at time t_i in a local extreme (see Fig. 10).

Decay experiments are analyzed by assuming that the measured data of each half cycle can be approximated to the theoretical solution of a damped linear single-DOF system. For example, Eq. (2) represents the motion of the uncoupled heave DOF in free vibration.

$$\ddot{z} + 2\mu_{eq,i}\dot{z} + \omega^2_{3,eq,i}\, z = 0 \tag{2}$$

where $\mu_{eq,i}$, is the equivalent linear damping coefficient expressed as

$$\mu_{eq,i} = \frac{B_{33,i}}{2 \cdot (M + A_{33,i})} \tag{3}$$

and $\omega_{3,eq,i}$ is the equivalent undamped circular natural frequency expressed as

$$\omega_{3,eq,i} = \sqrt{\frac{C_{33}}{M + A_{33,i}}} \tag{4}$$

where M, C_{33}, B_{33}, $A_{33,i}$ are the mass, stiffness, linear damping and added mass in heave, respectively. Assuming that the system is lightly damped, the solution of the motion model of Eq. (2) can be approximated by the following analytical solution:

$$z(\tau) = e^{-\mu_{eq,i}\cdot\tau} Z_i \cos(\omega_{3,d,i} \cdot \tau), \tag{5}$$

with $\tau = t - t_i$ and $\omega_{3,d,i}$ is the damped circular natural frequency expressed as

$$\omega_{3,d,i} = \sqrt{\omega^2_{3,eq,i} - \mu^2_{eq,i}} \tag{6}$$

Which can be determined approximately from the time between consecutive peaks:

$$\omega_{3,d,i} = \frac{\pi}{t_{i+1} - t_i} \tag{7}$$

By taking the logarithms of Eq. (5) for two consecutive peaks in the time interval $[t_i, t_{i+1}]$, the characteristic parameter $\mu_{eq,i}$ is given by:

$$\mu_{eq,i} = \frac{1}{t_{i+1} - t_i} \log\left(\frac{|Z_i|}{|Z_{i+1}|}\right) \tag{8}$$

Both are assumed to vary slowly across the decay cycles. Therefore, the mean values of all the analyzed half cycles can be selected as representative values [38].

Finally, the nondimensional damping ratio, ξ, is defined as a fraction of the critical damping, B^{crit}_{33}, as follows

$$\xi = \frac{\mu_{eq}}{\omega_{3,eq}} = \frac{B_{eq,33}}{B^{crit}_{33}} \tag{9}$$

Three repetitions for each decay test were performed and different amplitude magnitudes and heading directions were applied to minimize the error in the measurements.

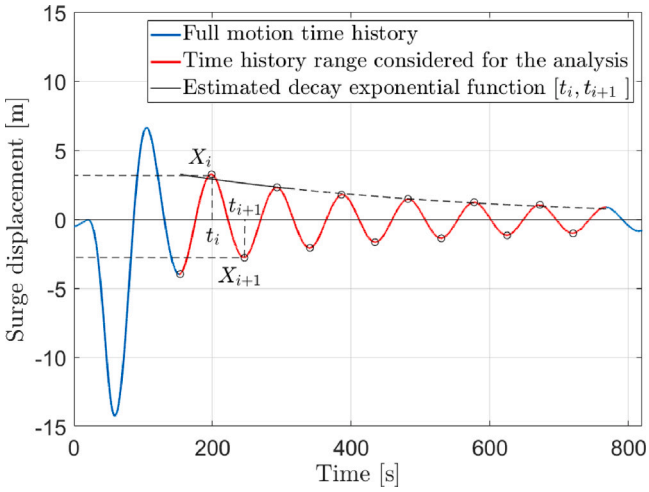

Fig. 10. Exemplied analysis of a decay time series.

Considering the 6-DOF rigid body motions of each FWT, the dual-spar FWF has twelve natural periods and corresponding eigenmodes [20]. In these eigenmodes, two FWTs move in the same heading or the opposite directions of a DOF. However, due to the difficulty of applying initial displacements or rotations to both FWTs to excite the eigenmodes, for the dual-spar FWF in the decay tests, an initial displacement or rotation was applied to Spar 1 only. The same experimental procedures as for the Single FWT are applied to the Dual-spar FWF, and natural periods and damping ratios of the FWT were estimated. In order to calibrate the multibody numerical models, we suggest that the viscous damping forces estimated from the single spar tests can be applied to each individual FWT of the FWF as a starting point. Then, numerical decay tests can be carried out for the FWF, and the obtained damping ratio and natural periods of the coupled modes will be compared with the experimentally measured ones. An iterative procedure may be needed to adjust the damping and drag coefficients of the system components (FWTs and mooring lines) to achieve a good match.

4.2. Wave tests

4.2.1. Wave calibration

All wave cases described in Section 3.3 were tested for both configurations following recommendations by the International Towing Tank Conference (ITTC) [39,40]. A calibration of the waves without the presence of the model was performed to ensure comparable wave loads between the two configurations.

According to ITTC [41], for irregular wave tests, a duration of 20–30 min at full scale is generally sufficient to collect statistically representative samples under wave-frequency responses. In this study, to obtain better response statistics with reduced statistical uncertainty [42], a duration of 1 h with three realizations is considered for each irregular sea state.

A comparison of the wave power spectrum density (PSD) between the theoretical and experimental results of the two irregular cases, with 3 seeds each, is presented in Figs. 11(a)–11(b). The calibration of the significant wave height (H_s) and the significant wave period (T_p) of the spectra are within acceptable errors (lower than 5%).

A white noise spectrum was also calibrated. This case was characterized by a target significant wave height H_s of 2 m and a frequency bandwidth between 0.05 and 0.20 Hz on full scale. Fig. 11(c) shows a comparison of the wave spectra between the theoretical and experimental results.

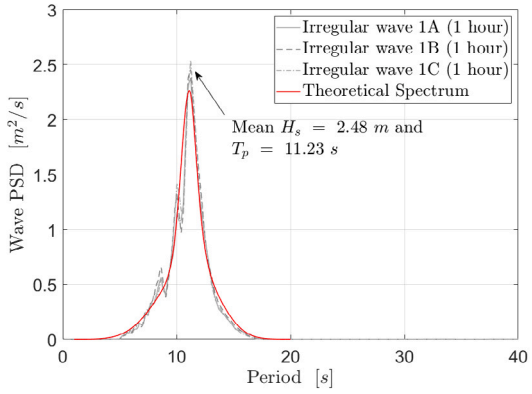

(a) Calibration of wave spectra; wave case IRR01.

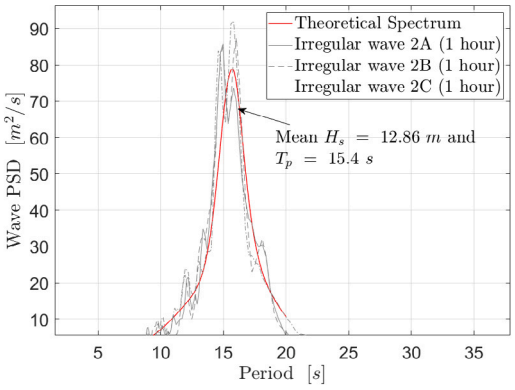

(b) Calibration of wave spectra; wave case IRR02.

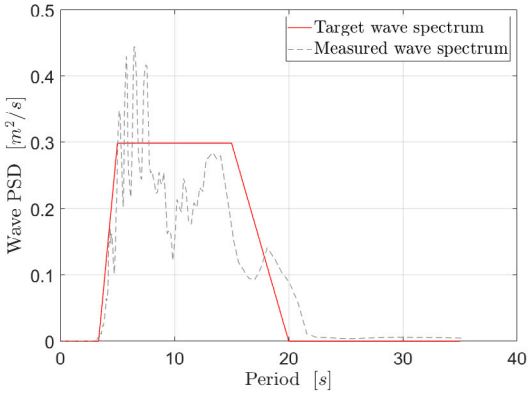

(c) Calibration of wave spectra; white noise case.

Fig. 11. Calibration of the wave power spectra.

The same quality criteria was adopted for the regular wave calibration, achieving an error of less than 5% for the wave height and period.

4.2.2. Response amplitude operators (RAOs)

In a linear hydrodynamic model, the response of the model (in motions and tensions) to regular waves is expected to be periodic with the same frequency as the incident wave. The forcing input of a regular wave with amplitude η_0 is expressed as follows:

$$\eta = \eta_0 \cos(\omega t) \tag{10}$$

Then, the output of a linear system is

$$X = X_0 \cos(\omega t + \epsilon_X) \tag{11}$$

Both the amplitude of the wave and the amplitude of the response were obtained with the first Fourier harmonic of the corresponding time series. The magnitude of the first-order RAO for a given frequency is calculated according to Eq. (12).

$$RAO_X(\omega) = \left| \frac{X_0}{\eta_0} \right| \tag{12}$$

The period and height of the calibrated regular waves tested have previously been shown in Table 7b. Between 10 and 20 cycles were used to determine the transfer function, following the ITTC recommendations [43].

Alternatively, signals of the calibrated white noise case are utilized to perform a frequency domain analysis of the model responses. Then, the RAO magnitudes can be determined according to Eq. (13) [36]. Here, S_{xy} and S_{xx} are the cross- and auto-spectral energy density spectra of the wave, respectively.

$$RAO_X = \frac{S_{xy}}{S_{xx}} \tag{13}$$

Units of the RAOs are m/m for translational motions, deg/m for rotational motions, t/m for tensions and forces, and t m/m for moments.

5. Results

Results will be presented focusing on a comparison between the two configurations explained in Section 3. In the figures, the single spar FWT and the dual-spar FWF are called “Single” and “Dual”, respectively. Fig. 12 shows snapshots of both configurations during the experiments; refer to Figs. 4–5 for the layout. The 0 deg wave heading is pointed in the figure with the light blue arrow. The estimated natural frequencies and damping ratios of the two configurations are presented in Section 5.1. RAOs are presented in Section 5.2. Finally, motions and mooring tension analysis for the irregular waves are conducted in Section 5.3. As only one wave heading is considered, the platform motion analysis focuses on surge, heave, and pitch.

5.1. Natural frequencies and damping of the two configurations

Following the procedure detailed in Section 4, the natural periods and damping ratios are estimated for both configurations and presented in Table 8. In line with the observations in [21], no significant differences between the two configurations are found for heave, roll, and pitch because these DOFs are hardly affected by the considered mooring configuration. Note that the most noticeable differences appear in the surge (51%) and sway (7%). This is due to the system reduction in stiffness by changing two anchor lines to a shared line in the dual configuration. Estimations of the average damping ratios ξ are listed in Table 9, showing no significant differences between the two configurations.

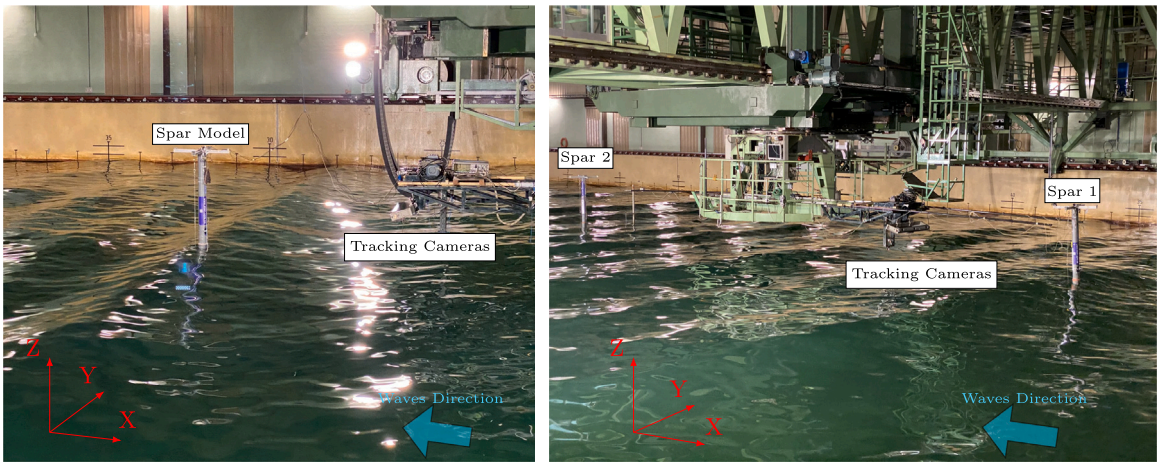

(a) Single-spar configuration. (b) Dual-spar configuration.

Fig. 12. Illustration of the two configurations during seakeeping tests. (For interpretation of the references to color in this figure legend, the reader is referred to the web version of this article.)

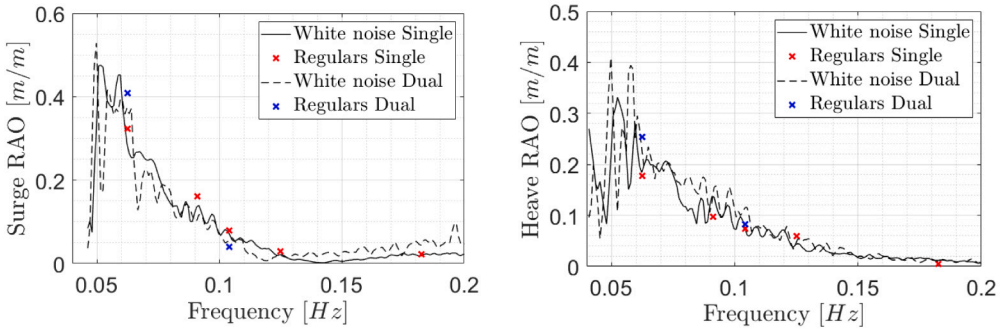

(a) Magnitude of the surge RAO. (b) Magnitude of the heave RAO.

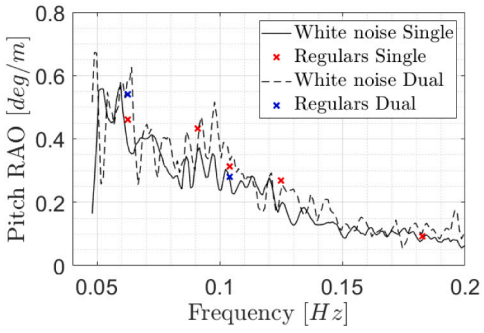

(c) Magnitude of the pitch RAO.

Fig. 13. Comparison of response amplitude operators for surge, heave and pitch motions, single- and dual-spar configurations.

Table 8
Natural period estimation for the two configurations [s].

	Surge	Sway	Heave	Roll	Pitch	Yaw
Single	93.03	87.92	29.80	31.69	31.71	24.55
Dual	142.88	83.89	30.50	31.56	31.32	23.93

Table 9
Estimation of the damping ratio ξ for the two configurations [%].

	Surge	Sway	Heave	Roll	Pitch	Yaw
Single	3.87	2.91	1.77	1.07	1.27	1.62
Dual	3.56	3.02	1.86	1.08	1.32	1.83

5.2. First-order RAOs from the regular wave and white noise tests

The estimated motion RAOs for both configurations are shown in Fig. 13. A comparison is presented between the white noise and the regular wave results, obtained based on methods described in Section 4.2.2. Generally, a good match between the two tests is achieved for both configurations. This is an indication of the system's linear behavior in this frequency range as energy is not transferred between different frequencies in the white noise tests.

Comparing the single- and dual-spar configurations, we observe that the differences between them are not substantial in the first-order frequency range. The reason is that the motion dynamics in this frequency range is not affected by the mooring used in this study.

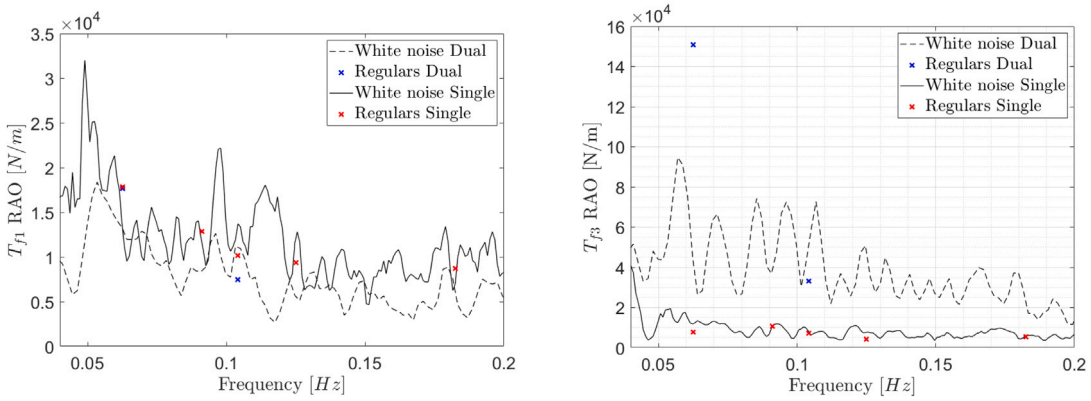

(a) T_{f1} RAO. (b) T_{f3} RAO.

Fig. 14. Comparison of response amplitude operators for anchor lines (T_{f1}) and shared line (T_{f3}); single- and dual-spar configurations.

As RAOs are just linear operators whereas the catenary mooring system has nonlinear restoring characteristics, the tension RAOs must be interpreted with caution. To evaluate the impact of the mooring system on tension responses, the tension RAOs have been estimated and are presented in Fig. 14. The results are similar for the anchor lines but substantial differences can be found for the shared line. A possible explanation is that since additional nonlinearities are present in an FWF with shared mooring (primarily due to the shared line), one can expect differences between the transfer function obtained from the white noise tests and from the regular wave. For a deeper investigation on this matter, more repetitions of these tests, and other white noise tests with different wave amplitudes and regular waves with different amplitudes and frequencies should be carried out. This has been left for future work.

5.3. Response analysis for the irregular wave tests

As discussed in Section 3.3, an operational and an extreme sea state have been tested. For FWTs in normal operation, aerodynamic loads have a significant impact on the motion and structural responses in addition to hydrodynamic loads. As wind loads were not considered during the tests, the studied load cases are representative of scenarios where the spar FWTs are parked due to maintenance or faults [44]. Under such scenarios, FWTs are usually parked with feathered blades and wave loads are dominant. To highlight the extreme responses of the FWF and to improve the narrative of the article, results of the operational condition are moved to Appendices B and C.

In order to present the results, first, motions will be analyzed, with a focus on surge motion, the crucial one in terms of the inter-array power cable design, and the one that is most affected by the change in the mooring configuration from “Single” to “Dual”. The platform-pitch motions will be also discussed as the floater’s tilt angle relates to serviceability limit state and is determined by tolerance requirements by turbine manufacturers. Mooring tensions will be discussed to close this section.

5.3.1. Motion responses

5.3.1.1. Spectral analysis. The PSDs are averaged across the three realizations of the surge motion in the extreme wave condition and are shown in Fig. 15. Individual PSD plots of the three realizations of the single- and dual-spar configurations are included in Appendix B.

As illustrated in Fig. 15, the surge motion PSDs have similar peaks in the first-order wave frequency range for both configurations despite clear differences in the low frequency range.

The surge-pitch coupling is evidenced by the peak around 30 s (0.033 Hz), which corresponds to the estimated natural period in pitch (see Table 8). This was also observed in Ramachandran et al. [45] and

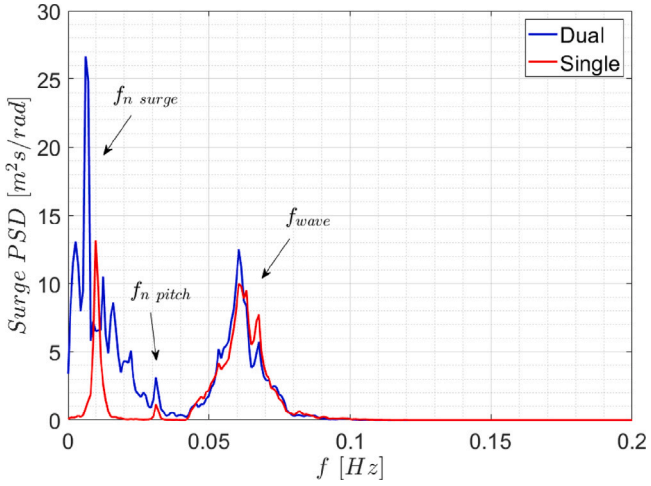

Fig. 15. Averaged surge spectra for the IRR02 wave case. H_s = 12.7 m and T_p = 15.45 s.

verified in other tests of spar FWTs, e.g., Meng et al. [46] and Yang et al. [47].

In the low-frequency range, surge resonant motions of both configurations are excited at peaks around 0.01 Hz; see Table 8. Compared with the single-spar configuration, the dual-spar configuration displays a larger amount of energy in periods 60 to 120 s (0.02 to 0.0075 Hz). This may be correlated with additional eigenmodes of the FWF due to the complex multibody dynamics present in the configuration, as discussed in Section 4.1 and in Liang et al. [20]. Future work is needed for a proper understanding of this particular energy distribution.

For the pitch DOF, the averaged PSDs are presented in Fig. 16(a) and are similar for both configurations. The differences in the heave motions between the two configurations are not large either (Fig. 16(b)). The reason for this observation is that both the heave and pitch motions are governed by the mass properties and the dominant hydrodynamic stiffness, while the mooring stiffness plays a secondary role.

Among the investigated DOFs, the surge motion is most affected by mooring configurations. Hence, one should focus on the surge offset when assessing the feasibility of the shared mooring in an FWF.

5.3.1.2. Statistics. A probability of exceedance (POE) curve measures the number of times a stochastic process exceeds some critical value per unit time. In the extreme sea state, excessive surge or pitch motions of the spar FWT may lead to damage of the inter-array power cables or drivetrain components. According to feedback from industrial partners in various initiatives, the experimentally obtained POEs can also be

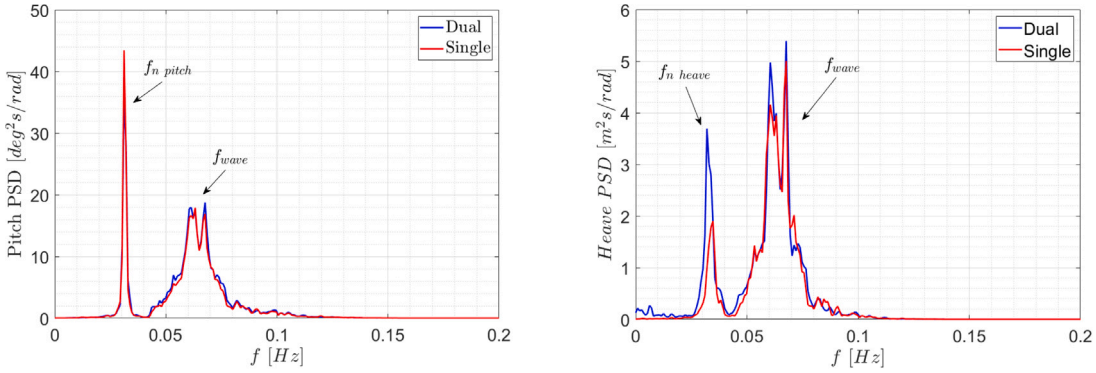

(a) Pitch (b) Heave

Fig. 16. Comparison of averaged pitch and heave spectra for the IRR02 wave case. H_s = 12.7 m and T_p = 15.45 s.

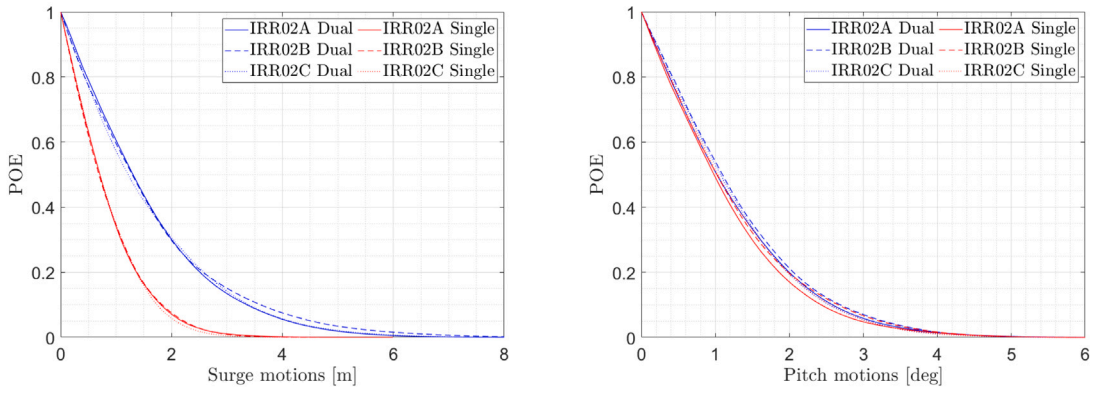

(a) Surge (b) Pitch

Fig. 17. POE of surge and pitch for the IRR02 wave case. H_s = 12.7 m and T_p = 15.45 s. (For interpretation of the references to color in this figure legend, the reader is referred to the web version of this article.)

useful in verification of numerical models for design and certification purposes. Hence, we use POE together with conventional statistics to compare the two configurations. Fig. 17 presents the POEs obtained from time histories of the surge and pitch motions for the three realizations. First, it is observed that the shapes of the POEs are consistent across the three realizations. Second, for a given level of POE, e.g., 0.1, the corresponding surge motion (blue curve) of the dual-spar configuration are significantly larger than that (red curve) of the single-spar configuration. This observation is consistent with previous observation for the surge PSDs. Additionally, the differences in the pitch motion POEs between the two configurations are negligible.

Eight statistical values of the surge and pitch motions are presented in Fig. 18 to facilitate a quantitative comparison of the two configurations. The design standards of FWTs, e.g., DNV-ST-0119 [35], require that the characteristic extreme responses for design are obtained by fitting probability models to the global maxima of each realization and for a sea state, many realizations should be simulated with different seeds. Due to the limited number of realizations from the experiments, we do not perform a design check but only compare the representative statistics.

As shown in Fig. 18(a), the total maxima and minima are mildly above the averaged maxima and minima for the surge motion for both configurations. This indicates a degree of stochastic uncertainty among the three realizations. Consistent with the POEs, there is larger maximum, mean, and RMS in surge for the dual-spar configuration than for the single-spar configuration. Such an observation is aligned with the numerical investigation [21]. For the mooring system design of FWF, there are no strict criteria regarding the maximum offset and a rule-of-thumb threshold is 10% of the water depth because of constraints of the inter-array power cables. For the present water depth, the maximum surge offset (approximately 8 m) of the dual-spar FWF is still below the threshold of 23.5 m.

It is interesting to notice that mean surge of the single spar FWT is substantially smaller than that of Spar1 of the FWF, whereas the RMS values of the two configurations are comparable. While the mean drift of the spars in the two configurations experiences a minor difference, the larger mean surge of the dual-spar configuration is mainly due to the reduced mooring stiffness in the surge direction as the shared line's contribution to the stiffness is relatively small.

Regarding the platform pitch motion, the two configurations display quite similar statistics, as shown in Fig. 18(b). The dual-spar configuration has slightly higher maximum and RMS than the single-spar configuration. This trend is consistent with the POEs presented before. Currently, the maximum allowable pitch angle in the range of 10–15 deg [48] is common for the nonoperational load cases, e.g., design load cases 6.1 and 6.2 in the IEC standard [49]. This design criterion is also fulfilled for both configurations in the extreme wave case.

5.3.2. Tension responses of the anchor lines

For both configurations, the fairlead tension T_{f1} (see Fig. 1) of one selected anchor line (Line 1) is focused on in the analysis. As Line 1 and Line 2 are symmetrical, the discussion for Line 2 is not included here.

5.3.2.1. Spectral analysis. As PSDs of individual realizations of the two configurations are included in Appendix C, the averaged PSD across the three realizations of the anchor line tensions for the extreme wave case is shown in Fig. 19. It is observed that the response in the first-order wave frequency range is more similar for both configurations

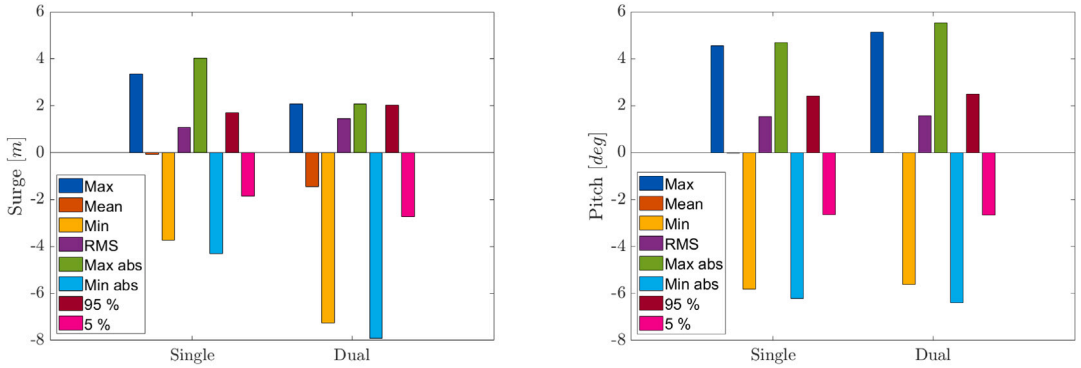

(a) Surge (b) Pitch

Fig. 18. Comparison of surge and pitch motion statistics for the IRR02 wave case. H_s = 12.7 m and T_p = 15.45 s. The statistical values are averaged across three realizations except "Max abs" and "Min abs". "Max abs": total maximum among three realizations; "Min abs": total minimum among three realizations; "Max": maximum; "Min": minimum; 'RMS": root mean square; "95%": 95% quantile; "5%": 5% quantile.

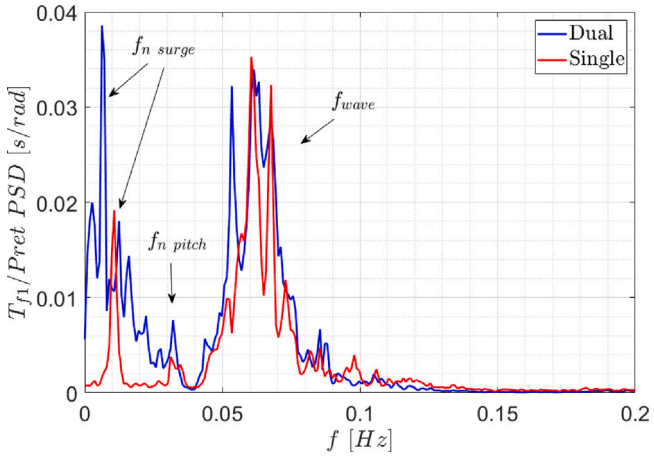

Fig. 19. Comparison of the anchor line tension PSDs for the IRR02 wave case. H_s = 12.7 m and T_p = 15.45 s.

than the response in the low frequency range. This is in line with the observations in Section 5.3.1.1 regarding the surge motion PSDs. In the low frequency range, the estimated natural surge periods and the surge-pitch coupling are also observed. In addition, a considerable amount of energy between 60–120 s (0.02 to 0.0075 Hz) is also be observed in the line tensions because of the correlation between the dynamic line tension and surge motions.

5.3.2.2. Statistics. Fig. 20 shows the POE curves of the time series of the fairlead tension, T_{f1}. In order to account for the different pretensions in the single- and dual-spar configurations, the statistics are normalized with the pretension. Similar to POEs of the motions in Section 5.3.1.2, these POEs can also be used in verification of numerical analysis results of mooring lines. As expected, the normalized T_{f1} fairlead tension POEs show relatively small variability across the three realizations for both configurations. This observation is similar to that of the surge or pitch motion. Generally, the tension POEs have similar trends in both configurations. For a given POE level, a moderately larger tension is observed for the dual-spar configuration.

As mentioned in Section 5.3.1.2, statistical quantities, e.g., the 5% and 95% quantiles, mean, and standard deviation, can be used to verify numerical models. Hence, these values for the fairlead tensions in the anchor lines are presented in Fig. 21. It is interesting to notice that the mean value of the fairlead tension is close to the pretension in both

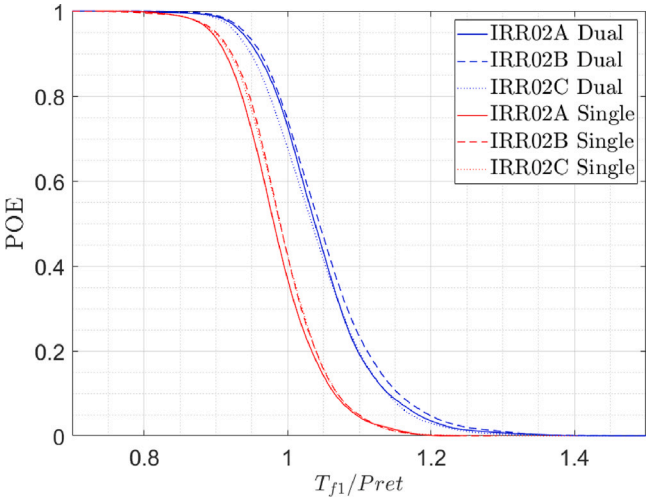

Fig. 20. Comparison of the anchor line tension POEs for the IRR02 wave case. H_s = 12.7 m and T_p = 15.45 s.

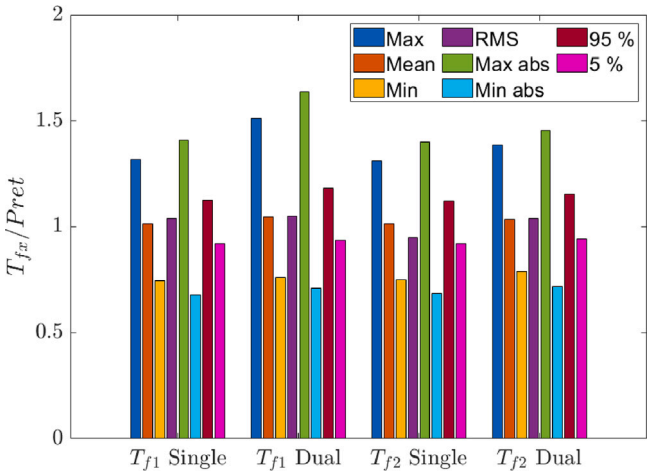

Fig. 21. Anchor lines tension statistics (normalized with the pretension) for the IRR02 wave case. H_s = 12.7 m and T_p = 15.45 s.

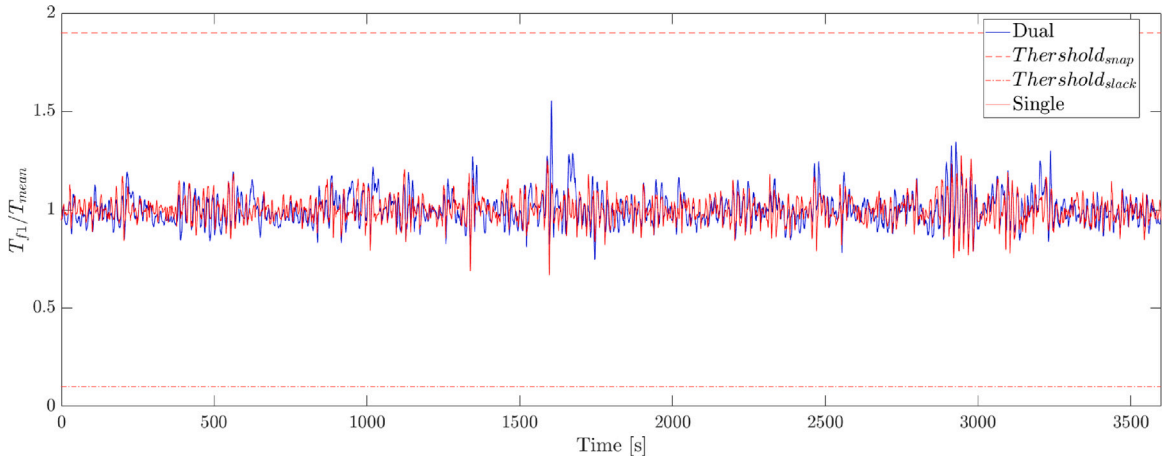

Fig. 22. Comparison of the anchor line tension in both configurations for extreme case IRR02B. The snap/slack thresholds and events are marked.

configurations, indicating that the mean drift in surge for the dual-spar FWF does not significantly impact the mean tension. This can be attributed to the reduced mooring stiffness in the FWF as discussed above. Among other quantities, the RMS and the 5% and 95% quantiles are slightly larger for the dual-spar configuration than for the single-spar configuration. This trend is consistent with the POEs shown in Fig. 20. Similar to the observation for the motions, the total maxima and minima of the three realizations are of the same order of the average maxima and minima.

Here, the discussion is focused on the extreme wave case. Results on the operational case and discussions on the differences in tension responses between Line 1 and Line 2 are found in Appendix C.

5.3.3. Tension responses of the shared line

Because the dynamics of the shared line is different from that of the anchor lines, the fairlead tensions in the shared line should be analyzed separately. This difference was shown when analyzing tension RAOs in Section 5.2 and can be clearly appreciated by observing the time histories for the extreme wave condition for the anchor lines and shared line for the single- and dual-spar configurations, as presented in Figs. 22–23.

When analyzing the dynamic mooring tensions, an interesting factor to consider is the snap events. According to Hsu et al. [50], a snap event can be described as a sudden and violent increase in tension that appears after a slack in the line. They proposed the following snap criteria based on the DNV guideline [51]:

$$T_{slack} \leq 0.1 \cdot T_{mean} \quad ; \quad T_{snap} \geq 1.9 \cdot T_{mean} \tag{14}$$

where T_{slack} is the local tension minima, T_{snap} is the local tension maxima, and T_{mean} is the mean dynamic tension.

In Figs. 22 and 23 the snap and slack events and their thresholds are highlighted following the above criteria. As shown in Fig. 22, for the anchor lines in both configurations, the thresholds (dashed lines) are far from the maximum ranges of the tension time histories. In contrast, for the shared line, a number of snap and slack events can be identified; see Fig. 23. Snap events experienced by the shared line were also reported in the previous numerical study [21] . As the present dual-spar FWF has one shared line, there is a significant reduction in the mooring stiffness in surge. In addition, the motions of Spar 1 and Spar 2 are not in phase in irregular waves and the relative distance between them varies. These factors contribute to the observed snap/slack events. Oscillations in the shared line tension due to these events are critical for the mooring design.

5.3.3.1. Spectral analysis. The average PSD and the PSDs of the three realizations for the shared line tension T_{f3} time histories are presented in Fig. 24. Consistency in the PSDs across the three realizations can be observed. Interestingly, unlike the PSDs of the anchor line tension (see

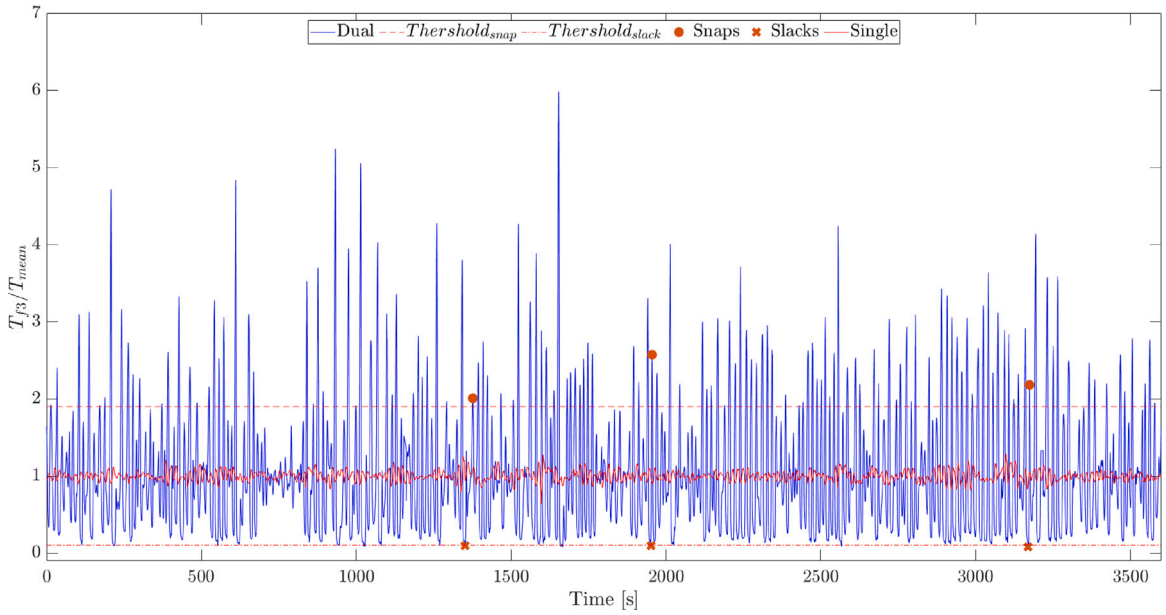

Fig. 23. Comparison of the shared line tension in the dual configuration and the equivalent fairlead in the single configuration for extreme case IRR02B. The snap/slack thresholds and events are marked.

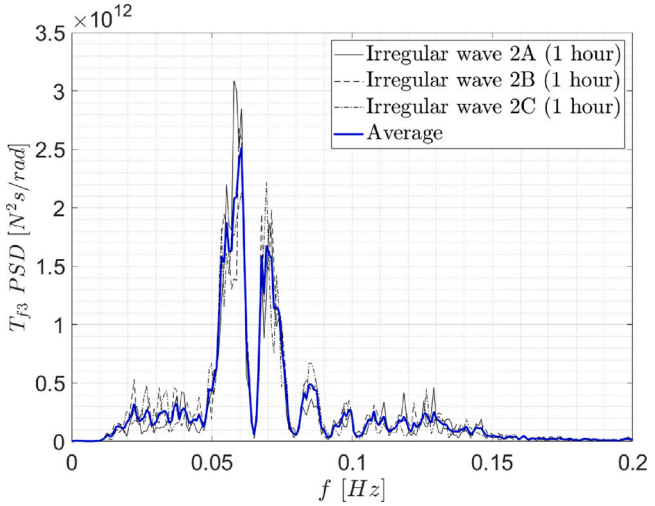

Fig. 24. Shared line fairlead tension T_{f3} PSD for the extreme IRR02 wave case. H_s = 12.7 m and T_p = 15.45 s.

Section 5.3.1.1), the PSD of the shared line tension displays peaks in the first-order wave frequency range (5–20 s). This observation agrees with Fig. 13 of a numerical study for an array of spar FWTs by Wang et al. [22].

5.3.3.2. Statistics. Fig. 25 shows POEs of the times series of the shared line tension T_{f_3} in the extreme irregular wave case. The grey zone refers to the region where the line tension is within the thresholds of the slack/snap criteria; refer to Eq. (14).

Regarding the snap events, one can observe that the shared line tension T_{f_3} exceeds the snap threshold during 15% of the time. Regarding slack events, the occurrence rate is far lower.

POEs of the peak tensions (maxima and minima) are presented in Fig. 26. It is remarkable that approximately 30% of the peaks are above the snap-event threshold and 5% are below the slack-event threshold. The frequent occurrence of the snap events evidence should be addressed to avoid premature failure of the shared line due to fatigue or mooring breakage. One strategy to reduce the likelihood of these events is to include clump weights in the lines, as Cabrerizo et al. [52] studied in the context of offshore operations. A detailed analysis of this approach for a shared mooring system for FWFs can be found in Liang et al. [53].

Statistics of the shared line tension are presented in Fig. 27. As shown, the normalized value of the maximum tension exceeds five. Compared with the anchor line (see Fig. 21), the shared line displays a higher level of dynamic tension and the difference between the maximum tension and the 95% quantile grows larger, which is aligned with the findings in [21]. As the large peak tensions and dynamic tensions are associated with the snap events, a proper design of the shared line with higher steel grade, increased wire diameter, or with additional mooring components can be carried out in future.

6. Conclusions

In this work, the dynamic performance of a dual-spar floating wind farm (FWF) with a shared line has been compared against a single floating wind turbine (FWT) with a catenary mooring system. To this aim, model-scale experiments were carried out at the INTA-CEHIPAR ocean basin in Madrid, Spain. The floater is the OC3-Hywind spar with a scale ratio of 1:47. Following discussions with industry advisors, a different water depth from that of the original Hywind is chosen (235 m instead of 320 m). Consequently, a different mooring system is proposed.

Natural periods and damping ratios have been estimated from decay tests. Two irregular wave conditions, a white noise, and five regular wave conditions have been tested. Only one wave heading has been tested, in which the shared line is collinear with the wave propagation direction. Response amplitude operators of motion and tension, motion and tensions spectra, and motion and tension statistics have been obtained under these conditions. To make the present effort more useful to the research community, the data discussed in the paper and videos of the experiments are made available (see "Data Availability section"). The main observations are listed as follows:

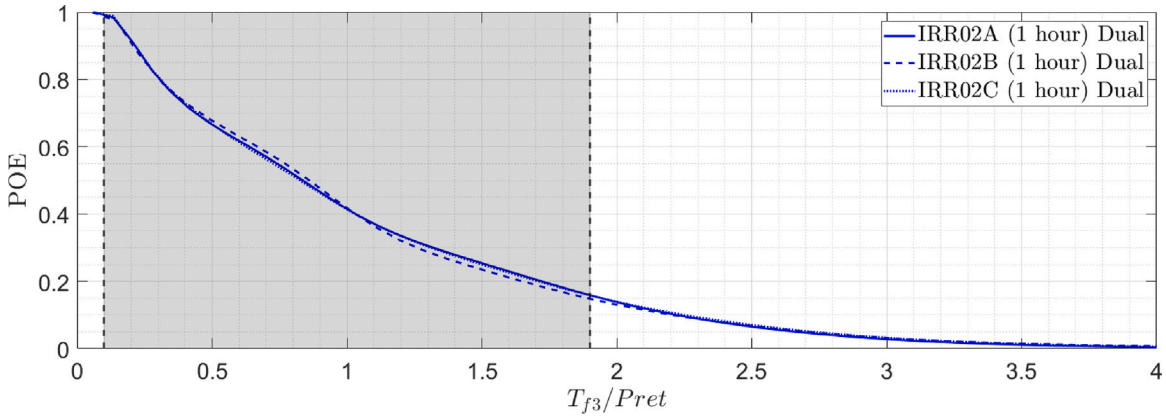

Fig. 25. POE of the time history of the shared line fairlead tensions T_{f_3} for the extreme IRR02 wave case. H_s = 12.7 m and T_p = 15.45 s.

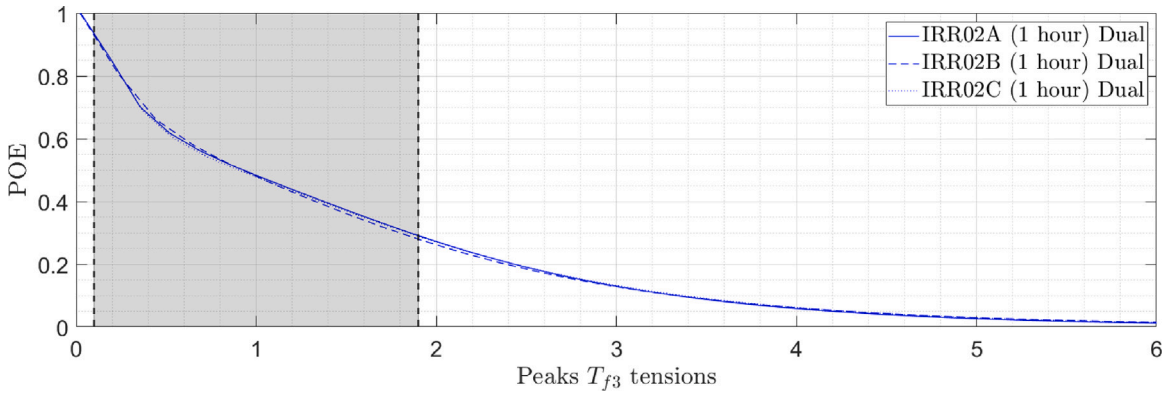

Fig. 26. POE of the peaks of the time history of the shared line fairlead tensions T_{f_3} for the extreme IRR02 wave case. H_s = 12.7 m and T_p = 15.45 s.

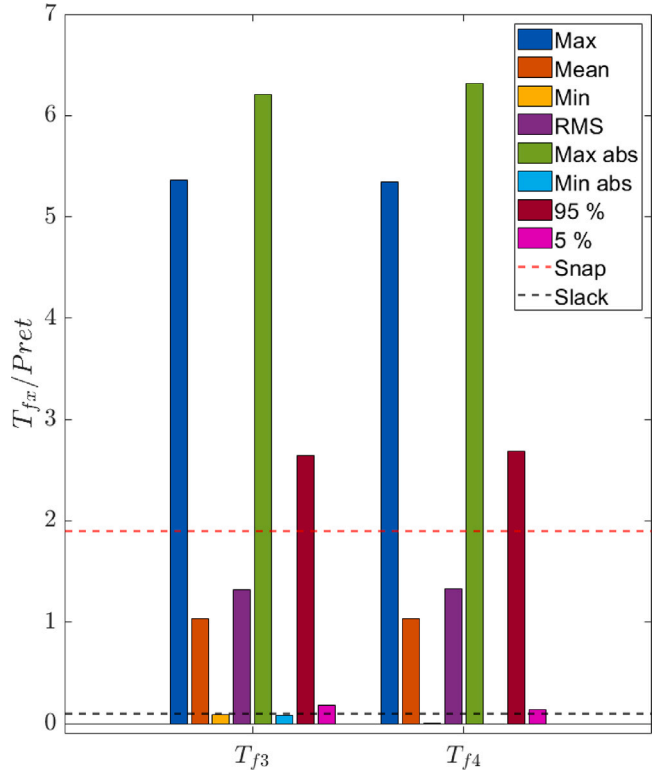

Fig. 27. Shared line fairlead tension statistics (normalized with the pretension) for the extreme sea state. IRR02 wave case. H_s = 12.7 m and T_p = 15.45 s.

- The surge natural period for the dual-spar configuration is 51% larger than that of the single spar configuration due to the change in mooring stiffness between the two configurations. The natural periods in heave and pitch experience small changes by moving to a shared mooring configuration. This is also expected as they are hardly affected by catenary mooring.
- Larger platform surge motion is observed for the dual-spar configuration than for the single-spar configuration. This fact is attributed to the reduction in the mooring stiffness due to the shared line. The platform heave and pitch motions remain similar between the two configurations. The proposed design criteria for surge (allowable offset of 10% water depth) and pitch (maximum 10 deg) are fulfilled in both configurations.
- Spectral analysis reveals that the shared line tension response has dominant peaks in the first-order wave frequency range.
- The tension responses in the anchor lines are of the same order and display no slack/snap events for both configurations, whereas large tension peaks, significant dynamic tension, and slack/snap events have been identified in the shared line in the FWF.

The results of this work help to better understand the complex multibody dynamics, and the performance of the highly attractive mooring solution as the shared mooring system. However, the scope of this work is limited. Future work may include testing of FWFs with additional instrumentation, conducting a number of static tests to estimate the mooring stiffness in the various degrees of freedom, generation of wind loads and combined load cases in the experiments, and improved design of the shared mooring systems.

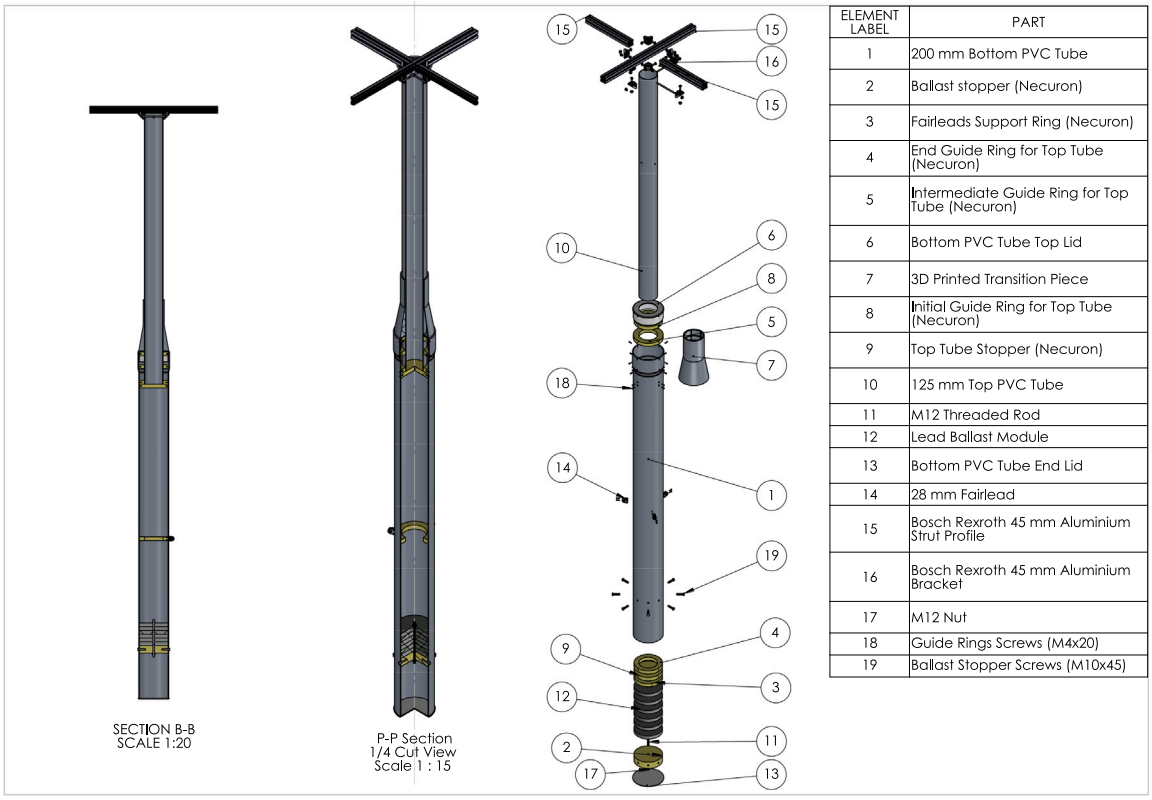

ELEMENT LABEL	PART
1	200 mm Bottom PVC Tube
2	Ballast stopper (Necuron)
3	Fairleads Support Ring (Necuron)
4	End Guide Ring for Top Tube (Necuron)
5	Intermediate Guide Ring for Top Tube (Necuron)
6	Bottom PVC Tube Top Lid
7	3D Printed Transition Piece
8	Initial Guide Ring for Top Tube (Necuron)
9	Top Tube Stopper (Necuron)
10	125 mm Top PVC Tube
11	M12 Threaded Rod
12	Lead Ballast Module
13	Bottom PVC Tube End Lid
14	28 mm Fairlead
15	Bosch Rexroth 45 mm Aluminium Strut Profile
16	Bosch Rexroth 45 mm Aluminium Bracket
17	M12 Nut
18	Guide Rings Screws (M4x20)
19	Ballast Stopper Screws (M10x45)

Fig. A.28. Design drawing of the model: component's view.

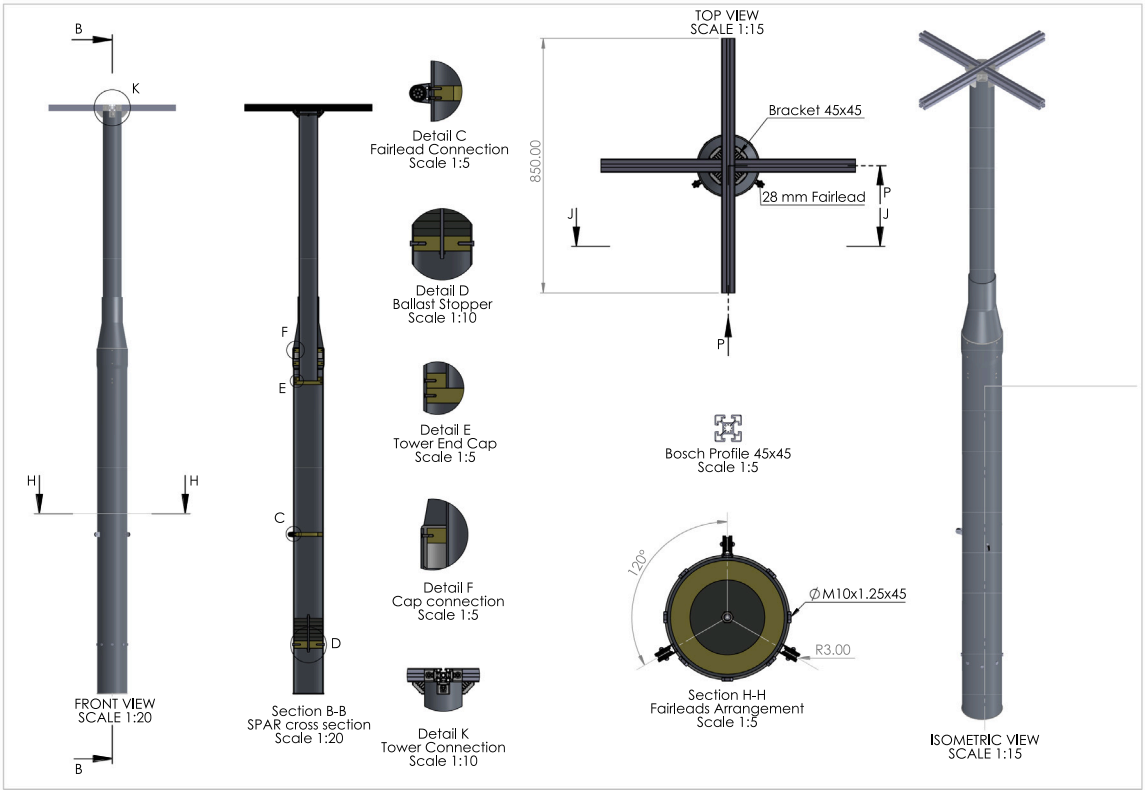

Fig. A.29. Design drawing of the model: external view.

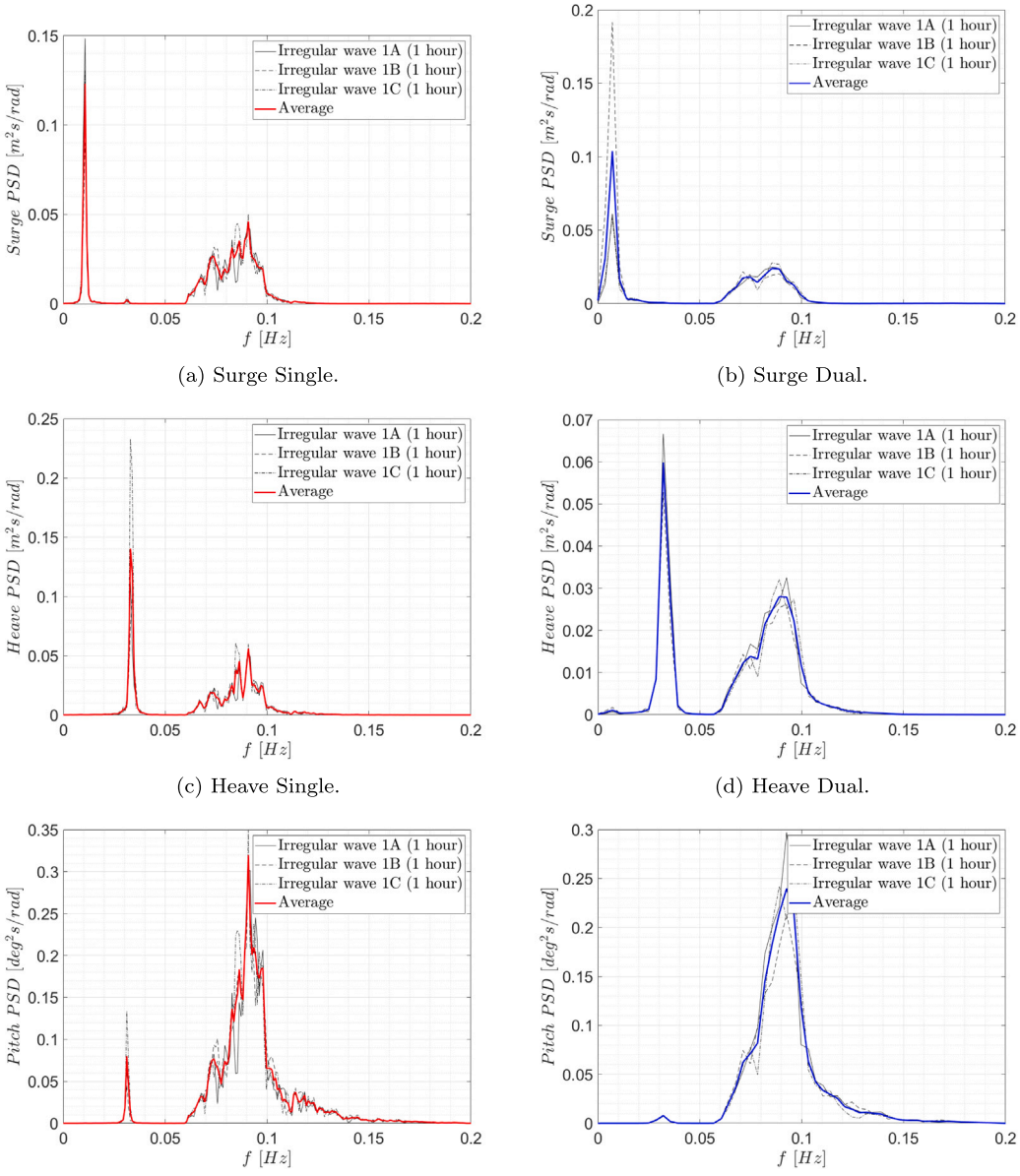

(a) Surge Single. (b) Surge Dual.

(c) Heave Single. (d) Heave Dual.

(e) Pitch Single. (f) Pitch Dual.

Fig. B.30. Surge, heave and pitch motion PSDs of all realizations and the average for both configurations. IRR01 (H_s = 2.57 m and T_p = 11.12 s).

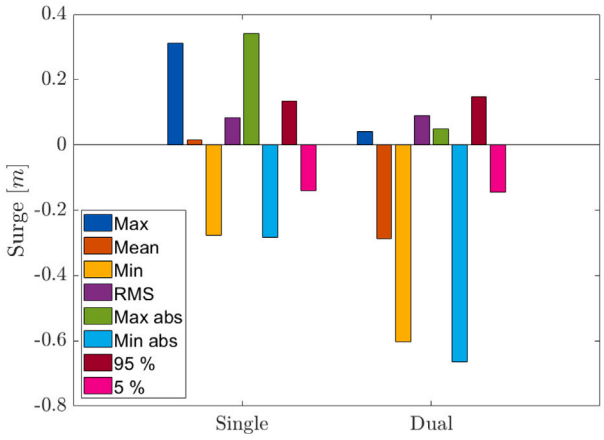

(a) Surge

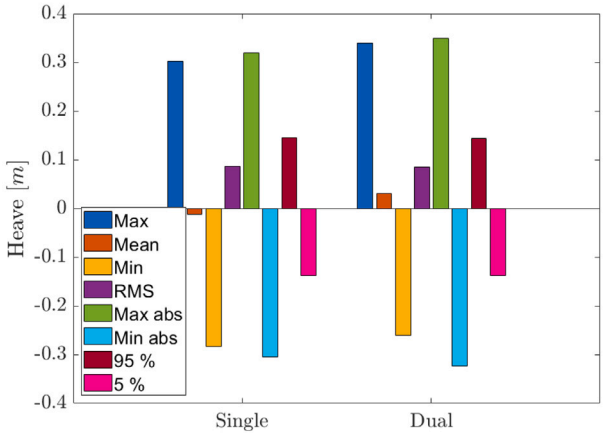

(b) Heave

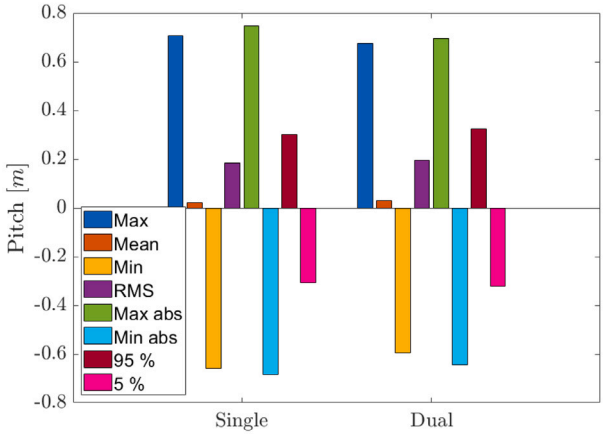

(c) Pitch

Fig. B.31. Comparison of surge, heave and pitch motion statistics for the IRR01 wave case ($H_s = 2.57$ m and $T_p = 11.12$ s).

CRediT authorship contribution statement

Tomas Lopez-Olocco: Investigation, Research, Methodology, Results discussion, Writing. **Guodong Liang:** Investigation, Research, Methodology, Results discussion, Writing. **Antonio Medina-Manuel:** Investigation, Discussion. **Leandro Saavedra Ynocente:** Investigation, Discussion. **Zhiyu Jiang:** Project management, Research methodology, Results discussion, Writing. **Antonio Souto-Iglesias:** Project management, Research methodology, Results discussion, Writing.

Declaration of competing interest

The authors would like to declare that the submitted paper has no conflict of interests with anyone else.

Data availability

The dataset used in the present study is made available on the server of CEHINAV Research Group (http://canal.etsin.upm.es/papers/lopezoloccoetal_sharedmooring_2023/).

Acknowledgments

The financial supports from UH-nett Vest (Project No. 720025) and ImpactWind SouthWest (Project No. 332034) are gratefully acknowledged. This research has also been partially funded by the Ministry of Science and Innovation of Spain through projects FWT-DAMP2 (Reference: PID2021-123437OB-C21) and FWT-PLATE-MOOR (Reference: TED2021-130951B-I00). Thanks are extended to Dr. Carlos Lopez-Pavon from COREMARINE SOLUTIONS, Spain and Prof. Simos from University of Sao Paulo, for fruitful discussions leading to the definition of some parameters of the tested configurations. The authors are also grateful to Javier Medina Galera for the assistance during the experimental campaign and for providing the sketch of the model design presented in Appendix A.

Appendix A. Design drawings of the tested models

Fig. A.28 shows the different labeled components used in the construction of the model. The main body is composed of two PVC tubes rigidly assembled together by means of a series of guides and PVC components. (Labels 4, 5, 6, 8 and 9). More details regarding the connections can be seen Details E and F of Fig. A.29. For the coned shaped transition part, a 3D-printed piece was used (Label 7).

Because of the low center of mass of the spar, an important amount of weight made of lead is placed at the bottom part (Label 12). This module is made of a series of lead disks, packed together with a screw. It was fixed to the bottom tube by means of 10 screws and supported by thick Necuron part (Label 2). More details of this connection can be seen in Detail D of Fig. A.29.

As mentioned in Section 3.1, the aluminum frame to reproduce the inertia properties as well to support the DAQ devices, is composed of three Bosch Rexroth extruded profiles (Label 15). The connection with the top tube can be seen in Detail K of Fig. A.29.

Also, as mentioned in Section 3.1 three pulleys were used as the fairlead connections (Label 14). Section H-H shows of Fig. A.29 the 120 deg arrangement. In addition, More details of this connection can be seen Detail C of Fig. A.29.

Appendix B. Motion responses: analysis through realizations

B.1. Operational sea state: IRR01 $H_s = 2.57$ m and $T_p = 11.12$ s

B.1.1. PSDs

PSDs are consistent across realizations and the differences in the low frequency range are attributed to the limited number of cycles for those frequencies (see Fig. B.30).

B.1.2. Statistics

See Fig. B.31.

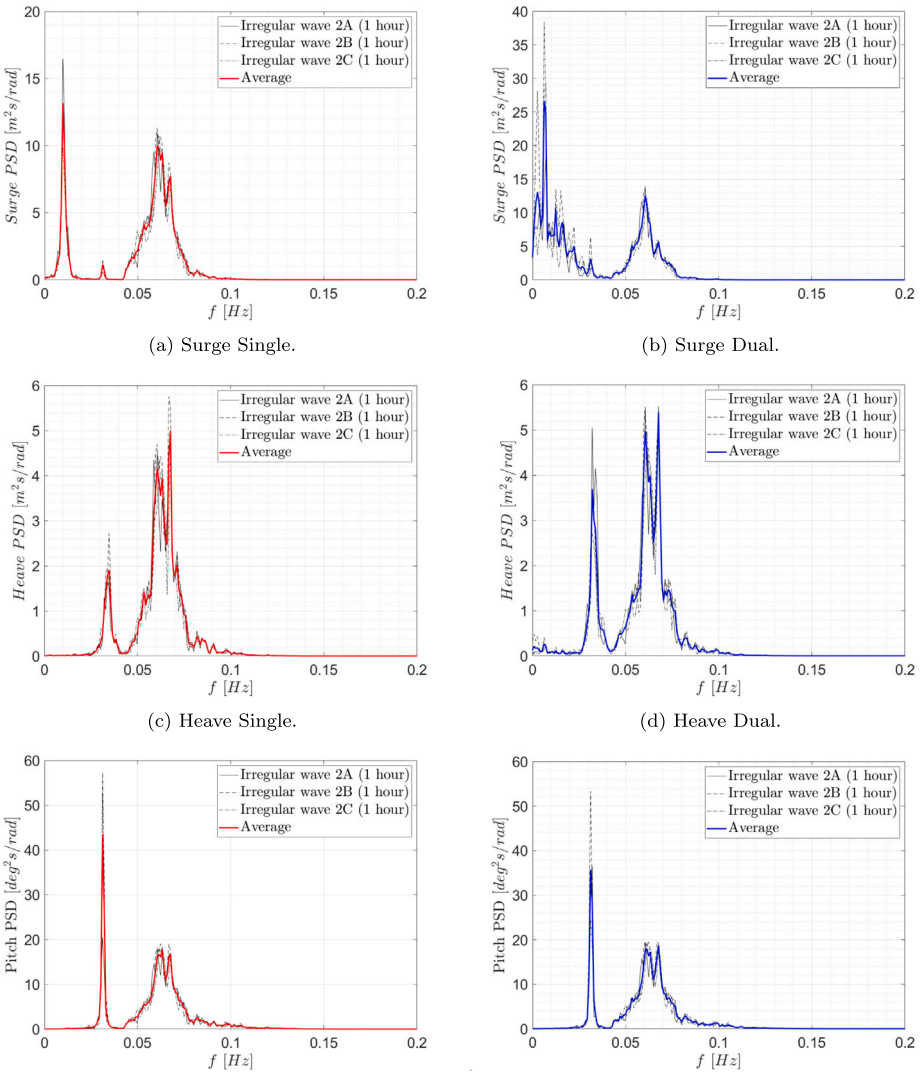

(a) Surge Single. (b) Surge Dual.

(c) Heave Single. (d) Heave Dual.

(e) Pitch Single. (f) Pitch Dual.

Fig. B.32. Surge, heave and pitch motion PSDs of individual realizations for the IRR02 wave case (H_s = 12.7 m and T_p = 15.45 s).

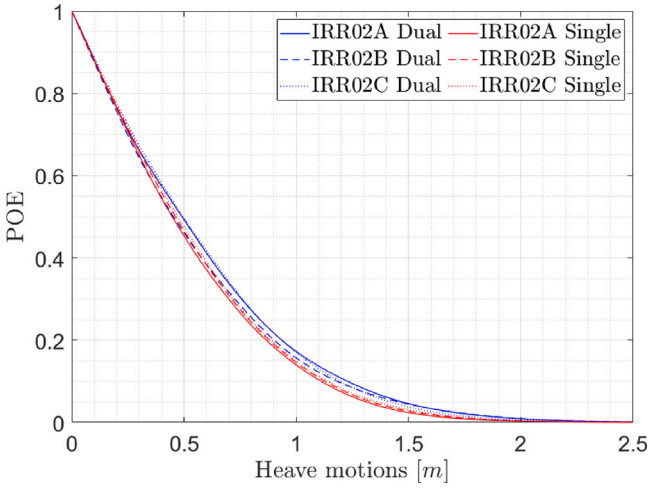

Fig. B.33. POE of heave for the IRR02 wave case (H_s = 12.7 m and T_p = 15.45 s).

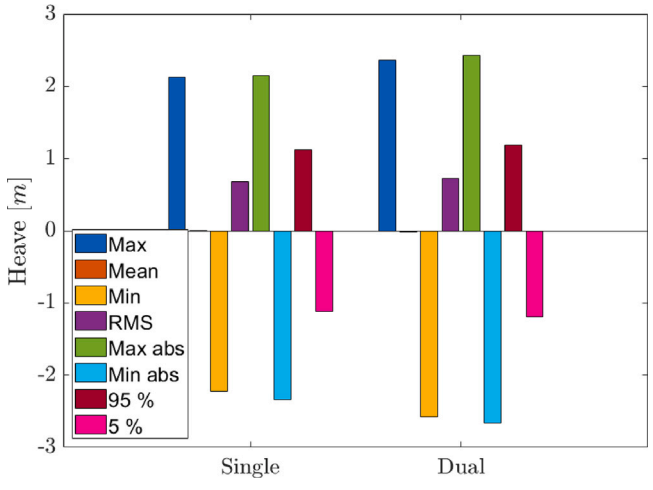

Fig. B.34. Comparison of heave motion statistics for the IRR02 wave case (H_s = 12.7 m and T_p = 15.45 s).

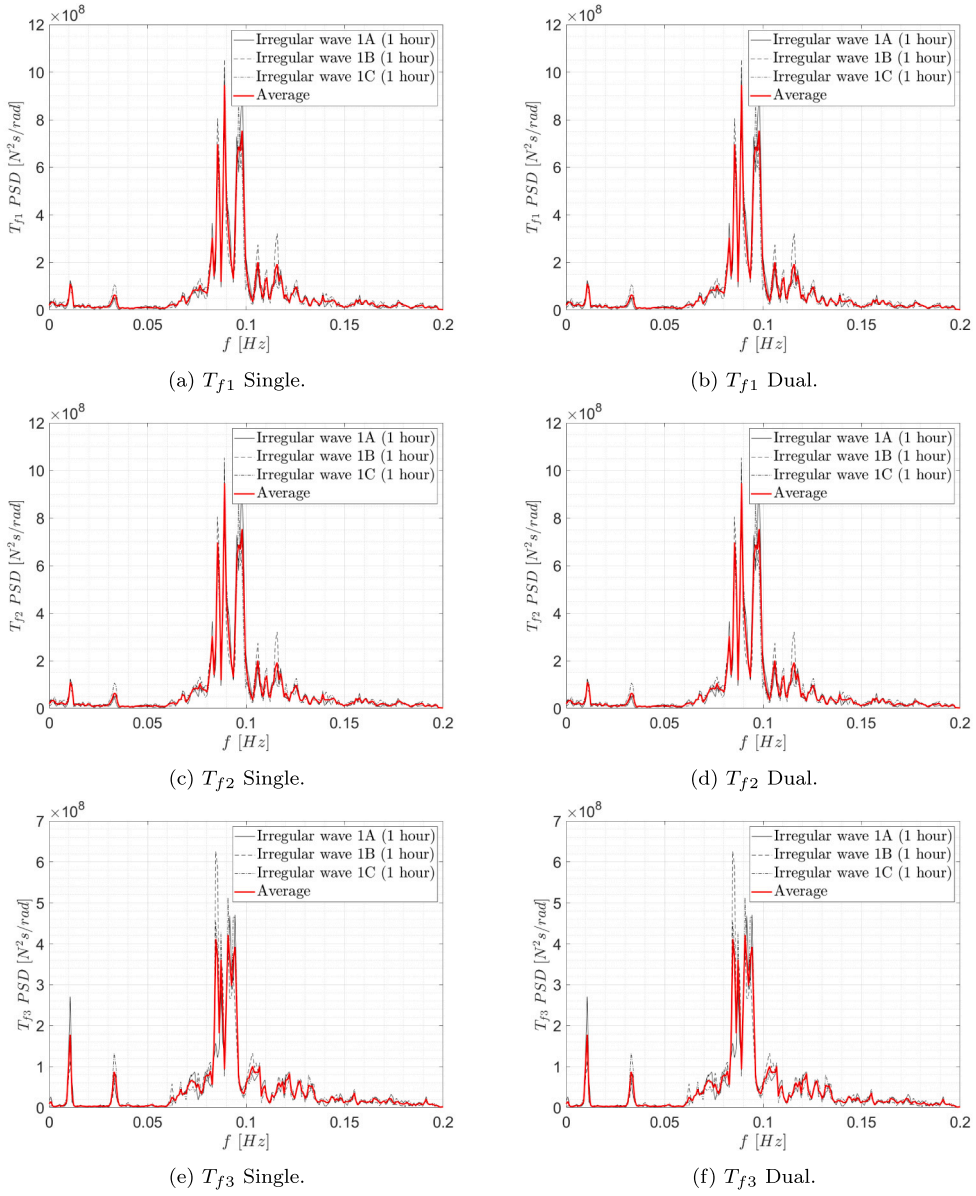

(a) T_{f1} Single. (b) T_{f1} Dual.

(c) T_{f2} Single. (d) T_{f2} Dual.

(e) T_{f3} Single. (f) T_{f3} Dual.

Fig. C.35. PSDs of individual realizations of mooring tensions (T_{f1}, T_{f2} and T_{f3}) for the IRR01 wave case (H_s = 2.57 m and T_p = 11.12 s).

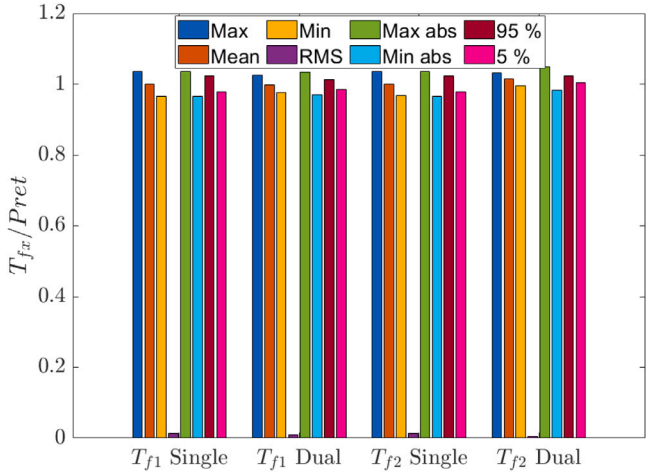

Fig. C.36. Statistics of anchor line tensions normalized against pretension for the IRR01 wave case (H_s = 2.57 m and T_p = 11.12 s).

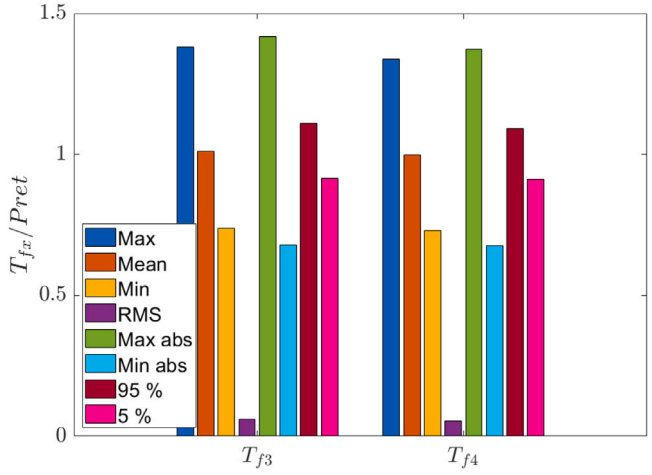

Fig. C.37. Statistics of shared line tensions normalized against pretension for the IRR01 wave case (H_s = 2.57 m and T_p = 11.12 s).

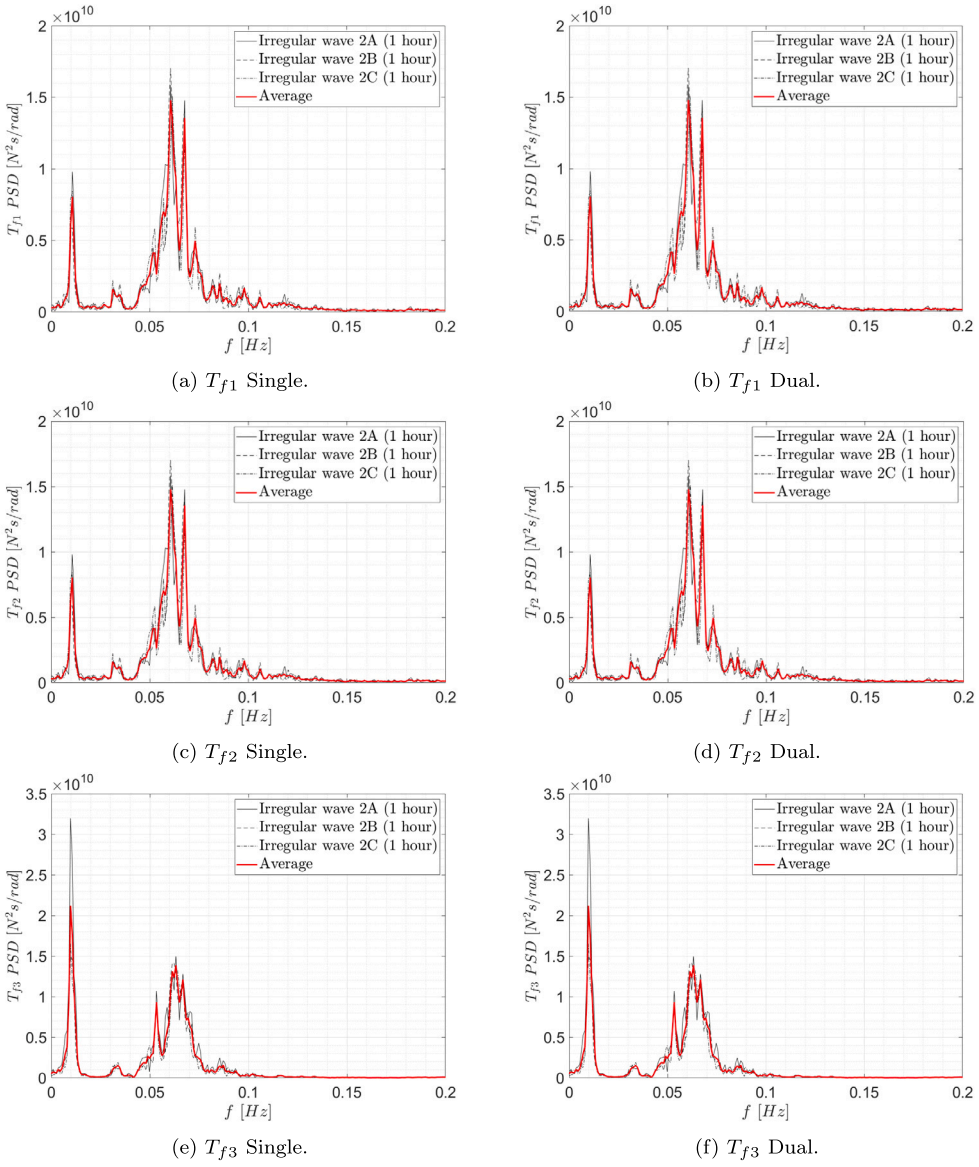

(a) T_{f1} Single. (b) T_{f1} Dual.

(c) T_{f2} Single. (d) T_{f2} Dual.

(e) T_{f3} Single. (f) T_{f3} Dual.

Fig. C.38. PSDs of individual realizations of mooring tensions (T_{f1}, T_{f2} and T_{f3}) for the IRR02 wave case (H_s = 12.7 m and T_p = 15.45 s).

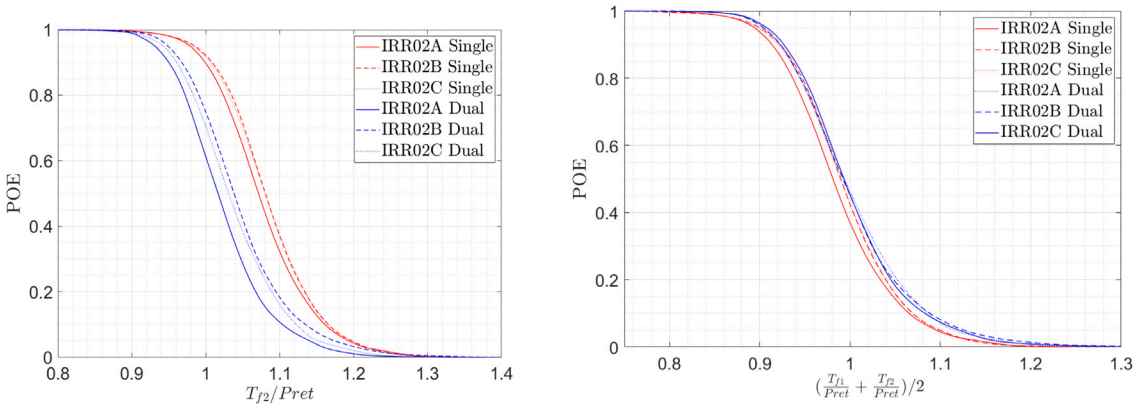

(a) T_{f2} normalized with the pretension (b) Averaged T_{f1} and T_{f2} normalized with the pretension.

Fig. C.39. Comparison of POEs of mooring tensions for the IRR02 wave case (H_s = 12.7 m and T_p = 15.45 s).

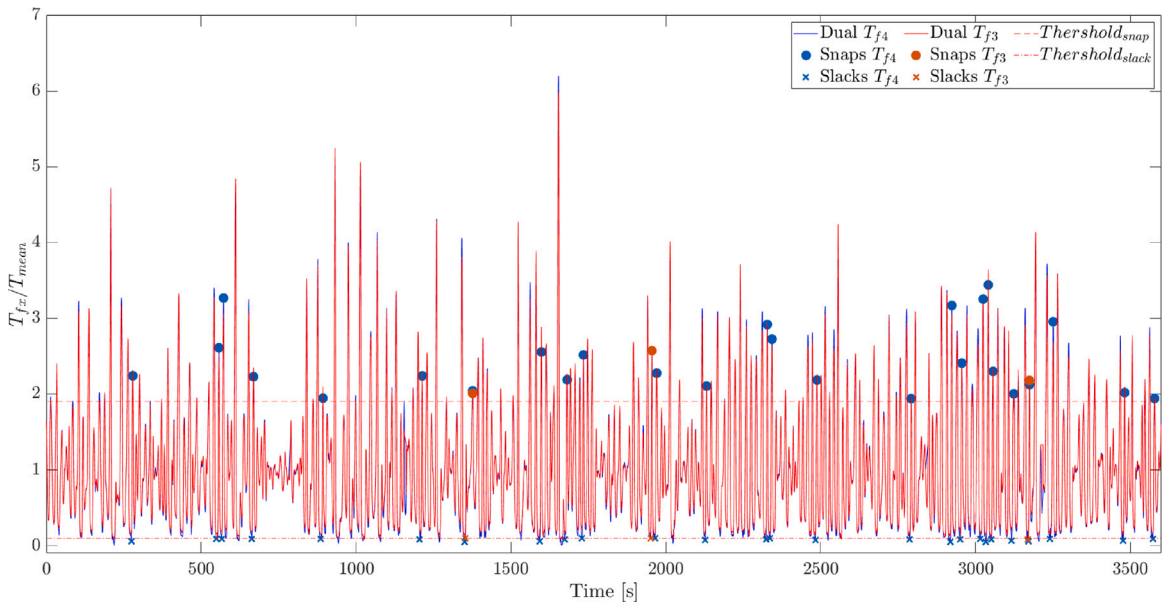

Fig. C.40. Fairlead tension T_{f3} and T_{f4} of the shared line for the wave case IRR02B. The snap/slack criteria and events are also shown.

B.2. Extreme sea state: IRR02 $H_s = 12.7$ m and $T_p = 15.45$ s

B.2.1. PSDs

PSDs are consistent across realizations and the differences in the low frequency range are attributed to the limited number of cycles for those frequencies (see Fig. B.32).

B.2.2. Statistics

Consistent with the observations in 5.3.1.2, the differences in the pitch motion POEs between the two configurations are also negligible in heave. This is shown in Fig. B.33

A similar consistency is shown in the statistics for this DOF in the extreme wave condition (see Fig. B.34).

Appendix C. Tensions responses: analysis through realizations

C.1. Operational sea state: IRR01 $H_s = 2.57$ m and $T_p = 11.12$ s

C.1.1. PSDs

PSDs are consistent across realizations and the differences in the low frequency range are attributed to the limited number of cycles for those frequencies (see Fig. C.35).

C.1.2. Statistics

Figs. C.36 and C.37 show the tension statistics for the anchor lines and shared line in the operational sea state. The fairlead tension statistics normalized with the pretension of the anchor lines are close to each other, when comparing both configurations. In the operational sea state, the shared line does not experience snap events, as described in 5.3.3.

C.2. Extreme sea state: IRR02 $H_s = 12.7$ m and $T_p = 15.45$ s

C.2.1. PSDs

PSDs are consistent across realizations and the dispersion in the low frequency range is attributed to the limited number of cycles for those frequencies (see Fig. C.38).

C.2.2. Statistics

C.2.2.1. Anchor lines. POEs of the fairlead tension for the other anchor line that was not presented in Section 5.3.2.2 (T_{f2}) are shown in Fig. C.39(a). Consistency across realizations is also appreciated in these figures. The considerable reduction of yaw stiffness for not using the delta connection explained in [28], together with minor errors in the construction of the model, might be accountable for differences that appear between T_{f1} and T_{f2} in the dual-spar configuration. In order to check the relevance of such lack of balance, Fig. C.39(b) shows POEs for the averaged fairlead tension T_{f1} and T_{f2}. As shown, when averaging both tensions, a good similarity with the Single configuration is found. It could be interesting in the future campaigns to assess the influence of the implementation of the delta connection on these disparities between anchor line tensions for the dual-spar configuration.

C.2.2.2. Shared line. Fig. C.40 shows a comparison between the fairlead tensions of the shared line in Spar 1 (T_{f3}) and Spar 2 (T_{f4}). As can be seen, the tensions response is similar for both fairleads. The same analysis described in Section 5.3.3 for the snap/slack condition has been performed. Some small differences are encountered in the peaks, and therefore more slack/snap events happen during the time histories. These differences appear to be caused by motions of the springs used to scale the stiffness of the line (see Table 5) during the experiments.

References

[1] An E. Strategy to harness the potential of offshore renewable energy for a climate neutral future. Brussels, Belgium: European Commission; 2020.
[2] Sannino G, Pisacane G, Carillo A, Struglia M. Strategic research Agenda towards innovation in Blue energy. 2019.
[3] Chakrabarti S. Handbook of offshore engineering (2-volume set). Elsevier; 2005.
[4] Skaare B, Nielsen FG, Hanson TD, Yttervik R, Havmøller O, Rekdal A. Analysis of measurements and simulations from the Hywind Demo floating wind turbine. Wind Energy 2015;18(6):1105–22.
[5] Nielsen FG, Hanson TD, Skaare B. Integrated dynamic analysis of floating offshore wind turbines. In: International conference on offshore mechanics and arctic engineering, Vol. 47462. 2006, p. 671–9.
[6] Tomasicchio GR, D'Alessandro F, Avossa AM, Riefolo L, Musci E, Ricciardelli F, Vicinanza D. Experimental modelling of the dynamic behaviour of a spar buoy wind turbine. Renew Energy 2018;127:412–32.

[7] Russo S, Contestabile P, Bardazzi A, Leone E, Iglesias G, Tomasicchio GR, Vicinanza D. Dynamic loads and response of a spar buoy wind turbine with pitch-controlled rotating blades: An experimental study. Energies 2021;14(12):3598.
[8] Myhr A, Maus KJ, Nygaard TA. Experimental and computational comparisons of the OC3-HYWIND and Tension-Leg-Buoy (TLB) floating wind turbine conceptual designs. In: The twenty-first international offshore and polar engineering conference. OnePetro; 2011.
[9] Goupee AJ, Koo BJ, Kimball RW, Lambrakos KF, Dagher HJ. Experimental comparison of three floating wind turbine concepts. J Offshore Mech Arct Eng 2014;136(2):020906.
[10] Koo BJ, Goupee AJ, Kimball RW, Lambrakos KF. Model tests for a floating wind turbine on three different floaters. J Offshore Mech Arct Eng 2014;136(2).
[11] Stehly T, Beiter P, Duffy P. 2019 cost of wind energy review. Technical report, Golden, CO (United States): National Renewable Energy Lab.(NREL); 2020.
[12] Pantusa D, Tomasicchio G. Large-scale offshore wind production in the Mediterranean Sea. Cogent Eng 2019;6(1):1661112.
[13] Devin MC, DuPont BL, Hallowell ST, Arwade SR. Optimizing the cost and reliability of shared anchors in an array of floating offshore wind turbines. ASCE-ASME J Risk Uncertain Eng Syst B Mech Eng 2021;7(4).
[14] Fontana C, Arwade S, DeGroot D, Hallowell S, Aubeny C, Diaz B, Landon M, Ozmutlu S, Myers A. Force dynamics and stationkeeping costs for multiline anchor systems in floating wind farms with different spatial parameters. In: International conference on offshore mechanics and arctic engineering, Vol. 58899. American Society of Mechanical Engineers; 2019, V010T09A079.
[15] Fontana CM, Arwade SR, DeGroot DJ, Myers AT, Landon M, Aubeny C. Efficient multiline anchor systems for floating offshore wind turbines. In: International conference on offshore mechanics and arctic engineering, Vol. 49972. American Society of Mechanical Engineers; 2016, V006T09A042.
[16] Equinor. Hywind tampen: The world's first renewable power for offshore oil and gas. 2019, https://www.equinor.com/energy/hywind-tampen [Online; accessed 12-October-2022].
[17] Chitteth Ramachandran R, Desmond C, Judge F, Serraris J-J, Murphy J. Floating wind turbines: marine operations challenges and opportunities. Wind Energy Sci 2022;7(2):903–24.
[18] Sloan C, Hall M, Housner S, Lozon E, Sirnivas S. Shared mooring systems for deep-water floating wind farms. Technical report NYSERDA Contract 142869, Golden, CO (United States): National Renewable Energy Lab.(NREL); 2022.
[19] Liang G, Merz K, Jiang Z. Modeling of a shared mooring system for a dual-spar configuration. In: International conference on offshore mechanics and arctic engineering, Vol. 9: Ocean Renewable Energy. American Society of Mechanical Engineers; 2020.
[20] Liang G, Jiang Z, Merz K. Mooring analysis of a dual-spar floating wind farm with a shared line. J Offshore Mech Arct Eng 2021;143(6):062003.
[21] Liang G, Jiang Z, Merz K. Dynamic analysis of a dual-spar floating offshore wind farm with shared moorings in extreme environmental conditions. Marine Structures 2023;90:103441.
[22] Wang Y, Wolgamot H, Watson P, Gaudin C, Zhao W, Milne I. Preliminary investigation of a shared mooring arrangement for a floating offshore wind turbine farm in deep water. In: International Conference on Offshore Mechanics and Arctic Engineering. 85932, American Society of Mechanical Engineers; 2022, p. V008T09A061.
[23] Wilson S, Hall M, Housner S, Sirnivas S. Linearized modeling and optimization of shared mooring systems. Ocean Eng 2021;241:110009.
[24] Goldschmidt M, Muskulus M. Coupled mooring systems for floating wind farms. Energy Procedia 2015;80:255–62.
[25] Hall M, Connolly P. Coupled dynamics modelling of a floating wind farm with shared mooring lines. In: International conference on offshore mechanics and arctic engineering, Vol. 51319. American Society of Mechanical Engineers; 2018, V010T09A087.
[26] Connolly P, Hall M. Comparison of pilot-scale floating offshore wind farms with shared moorings. Ocean Eng 2019;171:172–80.
[27] Lozon E, Hall M. Coupled loads analysis of a novel shared-mooring floating wind farm. Appl Energy 2023;332:120513.
[28] Jonkman J. Definition of the floating system for phase IV of OC3. Technical report NREL/TP-500-47535, Golden, CO (United States): National Renewable Energy Lab.(NREL); 2010.
[29] Jonkman J, Butterfield S, Musial W, Scott G. Definition of a 5-MW reference wind turbine for offshore system development. Technical report NREL/TP-500-38060, Golden, CO (United States): National Renewable Energy Lab.(NREL); 2009.
[30] Li L, Gao Z, Moan T. Joint distribution of environmental condition at five European offshore sites for design of combined wind and wave energy devices. J Offshore Mech Arct Eng 2015;137(3).
[31] DNV GL. MIMOSA-user's doumentation programme version 5.7. Høvik, Norway; 2003.
[32] SINTEF Ocean. RIFLEX 4.16.0 user guide. Trondheim, Norway; 2019.
[33] SINTEF Ocean. SIMO 4.16.0 user guide. Trondheim, Norway; 2019.
[34] Veritas DN. Position mooring, offshore standard os-e301. Technical report, DNV-OS-E301, 2008.
[35] DNV. DNV-ST-0119 floating wind turbine structures. Oslo, Norway; 2021.
[36] Chakrabarti SK. Offshore structure modeling, Vol. 9. world scientific; 1994.
[37] Barrera C, Guanche R, Losada IJ. Experimental modelling of mooring systems for floating marine energy concepts. Mar Struct 2019;63:153–80.
[38] Medina-Manuel A, Botia-Vera E, Saettone S, Calderon-Sanchez J, Bulian G, Souto-Iglesias A. Hydrodynamic coefficients from forced and decay heave motion tests of a scaled model of a column of a floating wind turbine equipped with a heave plate. Ocean Eng 2022;252:110985.
[39] ITTC. Recommended procedures and guidelines: Seakeeping experiments. 2017.
[40] ITTC. Recommended procedures and guidelines: Model tests for offshore wind turbines. 2017.
[41] ITTC. Recommended procedures and guidelines: Floating offshore platform experiments. 2017.
[42] DNV GL. DNVGL-RP-0286: Coupled analysis of floating wind turbines. Recommend practice DNVGL-RP-0286, Oslo, Norway: DNV GL; 2019.
[43] ITTC. Recommended procedures and guidelines: Analysis procedure for model tests in regular waves. 2017.
[44] Jiang Z, Karimirad M, Moan T. Response analysis of parked spar-type wind turbine considering blade-pitch mechanism fault. Int J Offshore Pol Eng 2013;23(02).
[45] Ramachandran G, Robertson A, Jonkman J, Masciola MD. Investigation of response amplitude operators for floating offshore wind turbines. In: The twenty-third international offshore and polar engineering conference. OnePetro; 2013.
[46] Meng L, He Y-p, Zhao Y-s, Yang J, Yang H, Han Z-l, Yu L, Mao W-g, Du W-k. Dynamic response of 6MW spar type floating offshore wind turbine by experiment and numerical analyses. China Ocean Eng 2020;34(5):608–20.
[47] Yang J, He Y-P, Zhao Y-S, Shao Y-L, Han Z-L. Experimental and numerical studies on the low-frequency responses of a spar-type floating offshore wind turbine. Ocean Eng 2021;222:108571.
[48] Pereyra BT, Jiang Z, Gao Z, Andersen MT, Stiesdal H. Parametric study of a counter weight suspension system for the tetraspar floating wind turbine. In: International conference on offshore mechanics and arctic engineering, Vol. 51975. American Society of Mechanical Engineers; 2018, V001T01A003.
[49] IEC. 61400-3-1. Wind energy generation systems Part 3-1: Design requirements for fixed offshore wind turbines. 2019, IEC 61400-3-Ed. 1.0.
[50] Hsu W-t, Thiagarajan KP, Manuel L. Extreme mooring tensions due to snap loads on a floating offshore wind turbine system. Mar Struct 2017;55:182–99.
[51] DNV. DNV-RP-H103: modelling and analysis of marine operations. HøVik, Norway: Det Norske Veritas; 2011.
[52] Cabrerizo-Morales M, Molina-Sanchez R, Pérez-Rojas L. Small-scale study of mooring line tension thresholds based on impulsive load analysis during big floating structure operation and commissioning. Water 2021;13(8):1056.
[53] Liang G, Lopez-Olocco T, Medina-Manuel A, Ynocente LS, Souto-Iglesias A, Jiang Z. Experimental investigation of two shared mooring configurations for a dual-spar floating offshore wind farm in irregular waves. 2022, Submitted for publication.